Evaluating modelled tropospheric columns of CH_4, CO and O_3 in the Arctic using ground-based FTIR measurements

Victoria A Flood[1], Kimberly Strong[1], Cynthia H. Whaley[2], Kaley A. Walker[1], Thomas Blumenstock[3], James W. Hannigan[4], Johan Mellqvist[5], Justus Notholt[6], Mathias Palm[6], Amelie N. Röhling[3], Stephen Arnold[7], Stephen Beagley[8], Rong-You Chien[9], Jesper Christensen[10], Makoto Deushi[11], Srdjan Dobricic[12], Xinyi Dong[9], Joshua S. Fu[9], Michael Gauss[13], Wanmin Gong[8], Joakim Langner[14], Kathy S. Law[15], Louis Marelle[15], Tatsuo Onishi[15], Naga Oshima[11], David A. Plummer[2], Luca Pozzoli[16,12], Jean-Christophe Raut[15], Manu A. Thomas[14], Svetlana Tsyro[13], and Steven Turnock[17, 7]

[1]Department of Physics, University of Toronto, Toronto, ON, Canada
[2]Canadian Centre for Climate Modelling and Analysis, Environment and Climate Change Canada, Victoria, BC, Canada
[3]Karlsruhe Institute of Technology, Institute of Meteorology and Climate Research (IMK-ASF), Karlsruhe, Germany
[4]Atmospheric Chemistry, Observations & Modeling, National Center for Atmospheric Research, Boulder, CO, USA
[5]Earth and Space Sciences, Chalmers University of Technology, Gothenburg, Sweden
[6]Institute of Environmental Physics, University of Bremen, Bremen, Germany
[7]Institute for Climate and Atmospheric Science, School of Earth and Environment, University of Leeds, Leeds, United Kingdom
[8]Air Quality Research Division, Environment and Climate Change Canada, Toronto, ON, Canada
[9]University of Tennessee, Knoxville, Tennessee, United States
[10]Department of Environmental Science/Interdisciplinary Centre for Climate Change, Aarhus University, Frederiksborgvej 399, 4000, Roskilde, Denmark
[11]Meteorological Research Institute, Japan Meteorological Agency, Tsukuba, Japan
[12]European Commission, Joint Research Centre, Ispra, Italy
[13]Division for Climate Modelling and Air Pollution, Norwegian Meteorological Institute, Oslo, Norway
[14]Swedish Meteorological and Hydrological Institute, Norrköping, Sweden
[15]Sorbonne Université, UVSQ, CNRS, LATMOS, Paris, France
[16]FINCONS SPA, Via Torri Bianche 10, 20871 Vimercate, Italy
[17]Met Office Hadley Centre, Exeter, UK

Correspondence to: Victoria A. Flood (v.flood@utoronto.com)

Abstract. This study evaluates tropospheric columns of methane, carbon monoxide, and ozone in the Arctic simulated by 11 models. The Arctic is warming at nearly four times the global average rate, and with changing emissions in and near the region, it is important to understand Arctic atmospheric composition and how it is changing. Both measurements and modelling of air pollution in the Arctic are difficult, making model validation with local measurements valuable. Evaluations are performed using data from five high-latitude ground-based Fourier transform infrared (FTIR) spectrometers in the Network for the Detection of Atmospheric Composition Change (NDACC). The models were selected as part of the 2021 Arctic Monitoring and Assessment Programme (AMAP) Report on Short-Lived Climate Forcers. This work augments the model-measurement comparisons presented in that report by including a new data source: column-integrated FTIR measurements whose spatial and temporal footprint is more representative of the free troposphere than in situ and satellite measurements. Mixing ratios of

Deleted: Both measurements and modelling of air pollution in the Arctic are difficult. Yet with

Deleted: This study examines the simulations of atmospheric concentrations of methane, carbon monoxide and ozone in the Arctic by 11 models.

trace gases are modelled at three-hourly intervals by CESM, CMAM, DEHM, EMEP MSC-W, GEM-MACH, GEOS-Chem, MATCH, MATCH-SALSA, MRI-ESM2, UKESM1 and WRF-Chem for the years 2008, 2009, 2014, and 2015. The comparisons focus on the troposphere (0-7 km partial columns) at Eureka, Canada; Thule, Greenland; Ny Ålesund, Norway; Kiruna, Sweden; and Harestua, Norway. Overall, the models are biased low in the tropospheric column, on average by -9.7% for CH_4, -21% for CO and -18% for O_3. Results for CH_4 are relatively consistent across the four years, whereas CO has a maximum negative bias in the spring and minimum in the summer, and O_3 has a maximum difference centred around the summer. The average differences for the models are within the FTIR uncertainties for approximately 15% of the model-location comparisons.

Deleted: 6

1 Introduction

Short Lived Climate Forcers (SLCFs) are a group of greenhouse gases and air pollutants with lifetimes less than two decades (IPCC, 2021). These include methane (CH_4), ozone (O_3), black carbon, halocarbons, sulfate, nitrate, and organic aerosols. The Intergovernmental Panel on Climate Change (IPCC) reports that in addition to radiative forcing, SLCFs have been found to have negative impacts on air quality, ecosystems, and human health. Due to their relatively short lifetimes, SLCFs are generally reflective of emission rates, meaning that mitigation can result in near-term impacts. Understanding the influences of SLCFs on the future climate will aid in policies and mitigation strategies to stay on track with the Paris Accord and its subsequent amendments. Reductions of SLCFs can be particularly beneficial in the Arctic because models have demonstrated a strong climate response in this region to local and remote forcing by SLCFs (Stohl et al., 2015).

Deleted: Furthermore, in most cases anthropogenic sources outweigh natural emissions and for SLCFs with shorter atmospheric lifetimes, less mixing occurs, causing most of the pollutants to remain predominantly localized.

Deleted: impact

The Arctic Monitoring and Assessment Programme (AMAP) was created by the Arctic Council to provide science-based analysis of Arctic pollution and climate change. AMAP has provided reports on SLCF impacts on the Arctic dating back to 2008. The 2021 AMAP SLCF Assessment Report assesses the impacts of black carbon, CH_4, O_3 and sulfate aerosols on the air quality, climate and human health in the Arctic region (AMAP, 2021). A key difference from previous AMAP reports is the emphasis on air quality and human health. In addition to these SLCFs, the analysis includes SLCF precursor gases carbon monoxide (CO), nitric oxide (NO) and nitrogen dioxide (NO_2). The report compares the output from 18 models with various historical measurements, including satellite, aircraft, ship, and in situ datasets. These observations are used to assess what processes need to be revised in the models and how these shortcomings impact the further application of the models, such as for climate and health predictions. Other chapters explore emissions, measurement advances, trends, climate air quality impacts, health ecosystem impacts, and next steps. A prominent theme in this report is the severity of change happening in the Arctic. This includes the amplification of the pace of change in physical drivers such as temperature and snow cover, and the frequency of extreme events, such as wildfires and incidents of rapid sea-ice loss. These factors contribute to ecosystem disruption, directly affecting local Arctic communities, in addition to having global repercussions. SLCF reductions are motivated by the near-term (20-30 years) benefits, and by the goal of slowing the warming of the Arctic climate, which results in more wildfires and permafrost melt, and in turn, an increase in SLCF emissions and precursor gases (AMAP, 2021). The

projections in this report provide guidance, objectives, and cautions for potential reduction implementation scenarios (AMAP, 2021). This study builds upon the model-measurement comparisons presented in the 2021 AMAP SLCF Assessment Report using an additional Arctic dataset that was not included in the original report.

The atmospheric measurements used to evaluate the models presented in this paper were made by Fourier transform infrared (FTIR) spectrometers that are contributing members of the Network for Detection of Atmospheric Composition Change (NDACC). NDACC has over 70 stations around the globe, collecting high-quality atmospheric composition measurements with ground-based, remote-sensing instruments (Kurylo and Soloman, 1990; De Mazière et al., 2018). The network's objective is to create a long-term database for various studies such as atmospheric trends, assessing links between climate, air quality and composition, and as a resource for other atmospheric investigations such as satellite validation and model development. Atmospheric vertical profiles and trace gas columns are retrieved from high-resolution FTIR spectrometers that record solar spectra featuring characteristic atmospheric absorption lines. Five of the 28 NDACC FTIR stations are located at latitudes north of 60°N, for the purpose of this study, these will all be referred to as Arctic sites. The five sites are; Eureka, Canada; Ny Ålesund, Norway; Thule, Greenland; Kiruna, Sweden; and Harestua, Norway. These high-latitude NDACC FTIR instruments provide a valuable set of long-term, measurements of multiple species of interest in the Arctic. Compared to surface in situ or satellite observations, the column-integrated FTIR measurements have a spatial and temporal footprint that is more representative of the free troposphere. Performing model-measurement comparisons with partial column data supports, thus complements, the assessments presented in the2021 AMAP Report. Previous studies have used FTIR data to examine model biases in the Arctic (e.g., Wespes et al., 2015; Zhou et al., 2019; Mahieu et al., 2021).

Measurements in the Arctic are difficult due to the harsh environment, remote locations, and high operating costs, resulting in a scarcity of monitoring stations and a limited representation of atmospheric vertical information. Using measurements to evaluate model simulations of the Arctic is important because the latter are used to project future changes in the Arctic, a region that is sensitive to climate change, warming at a rate three to four times the global average (Bush and Lemmen, 2019; NOAA, 2020; AMAP, 2021; IPCC, 2021; Rantanen et al., 2022). These factors have led to initiatives like the AMAP SLCF Assessment and the POLARCAT (Polar Study using Aircraft, Remote Sensing, Surface Measurements and Models, of Climate, Chemistry, Aerosols and Transport) Model Intercomparison Project (POLMIP) which, in part, aim to assess model performance in the Arctic region. POLMIP examined 11 atmospheric models in relation to a variety of Arctic observations taken as part of the International Polar Year in 2008 (Emmons et al., 2015). AMAP and POLMIP, in addition to the subsequent complementary publications (i.e., Wespes et al., 2012; Emmons et al., 2015; Monks et al., 2015; Whaley et al., 2022; 2023) provide a valuable point of reference for the modelling of CH_4, CO and O_3 in the Arctic, which is explored in this paper. This allows for the findings presented here to be appraised relative to results from the same models compared to other instruments, with differing temporal frequency and altitude ranges (i.e., Whaley et al., 2022; 2023), with different simulations and Arctic FTIR measurements (i.e., Wespes et al., 2015), and to generally assess the similarities/differences that arise within Arctic SLCF modelling.

Deleted: all of which are included in this study

Deleted: . All of these factors lead to

Deleted: ; as such, utilization of all available data sources is valuable in aiding model development.

This project examines simulations from 11 models that were run for the 2021 AMAP SLCF Assessment Report, to assess the agreement between modelled trace gas concentrations and ground-based retrievals from high-latitude FTIR spectrometers. Specifically, this paper presents comparisons of CH_4, CO and O_3 partial columns (from 0-7 km) for the years 2008, 2009, 2014, and 2015. The models examined are chemical transport and climate models: CESM, CMAM, DEHM, EMEP MSC-W, GEM-MACH, GEOS-CHEM, MATCH, MATCH-SALSA, MRI-ESM2, UKESM1 and WRF-CHEM. The objective is to utilize the high-quality, long-term Arctic FTIR datasets to assess how well the models perform. The remainder of this paper is organized as follows: Sect. 2 provides a description of the datasets used, Sect. 3 describes the analysis methodology, Sect. 4 examines the results and compares them with similar studies, and Sect. 5 presents the summary and conclusions.

2 Datasets

2.1 FTIR spectroscopy and retrievals

The FTIR measurement sites included in this study are summarized in Table 1 and the data is publicly available on the NDACC data repository [https://www-air.larc.nasa.gov/missions/ndacc/data.html]. These instruments require sunlight and a clear sight to the sun to make measurements, and so the high-latitude datasets are limited to the sunlit portion of the year at each location. To ensure high data quality and consistency between sites, NDACC has several specialized instrument and theme groups; the instruments used here are part of the Infrared Working Group (IRWG). The ten standard gases reported by sites participating in the IRWG are C_2H_6, CH_4, CO, $ClONO_2$, HCl, HCN, HF, HNO_3, N_2O, and O_3, while several other gases are retrieved as research data products, including C_2H_2, CH_3OH, H_2CO, HCOOH and OCS. The FTIR measurements cycle through a series of optical filters covering different spectral regions between approximately 650 and 4500 cm^{-1} for the retrieval of multiple atmospheric gases. Atmospheric trace gas profiles and columns are retrieved with the SFIT4 algorithm, using optimal estimation to iteratively adjust an a priori profile to match a modelled spectrum to the measured spectrum within a defined convergence criterion (Rodgers, 2000; IRWG, 2020). The a priori information for the modelled spectra is provided by 40-year-average profiles from the Whole Atmosphere Community Climate Model (WACCM) (Marsh et al., 2013), with spectroscopic absorption parameters from the HITRAN 2008 line-list (Rothman et al., 2009) and daily pressure and temperature profiles from the U.S. National Centers for Environmental Prediction (NCEP) (Kalnay et al., 1996). All sites included in this paper use SFIT4, except Kiruna, which uses a comparable retrieval code called PROFFIT, which has been shown to agree well with SFIT (Hase et. al, 2004). Primary references and further details of the sites are presented in Table 1.

Table 1: Summary of NDACC FTIR sites used in this study.

Site	Location	Key References	Operations

Deleted: The Network for Detection of Atmospheric Composition Change (NDACC) has over 70 stations around the globe, collecting high-quality atmospheric composition measurements with ground-based, remote-sensing instruments (Kurylo and Soloman, 1990; De Mazière et al., 2018). The network's objective is to create a long-term database for various studies such as atmospheric trends, assessing links between climate, air quality and composition, and as a resource for other atmospheric investigations such as satellite validation and model development. Atmospheric vertical profiles and trace gas columns are retrieved from high-resolution Fourier transform infrared (FTIR) spectrometers that record solar spectra featuring characteristic atmospheric absorption lines. Five of the 28 NDACC FTIR stations are located at latitudes north of 60°N, all of which are included in this study: Eureka, Canada; Ny Ålesund, Norway; Thule, Greenland; Kiruna, Sweden; and Harestua, Norway. ¶

Deleted: these

Deleted: This study builds upon the model-measurement comparisons presented in the 2021 AMAP SLCF Assessment Report using an additional Arctic dataset that was not included in the original report. …

Deleted: data

Deleted: program

Eureka, Canada	80.05°N, 86.42°W 610 masl	Batchelor et. al. (2009)	Late February to Mid-October
			Since 2006
Ny Ålesund, Norway	78.92°N, 11.93°E 15 masl	Notholt et al. (1997a,b); Notholt et al. (2000)	Mid-March to September
			Since 1992
Thule, Greenland	76.53°N, 68.74°W 225 masl	Hannigan et al. (2009)	March to October
			Since 1999
Kiruna, Sweden	67.84°N, 20.41°E 419 masl	Blumenstock et al. (1997, 2009)	Mid-January to November
			Since 1996
Harestua, Norway	60.2°N, 10.8°E 596 masl	Galle et al. (1999)	All Year
			Since 1994

The NDACC FTIR data files include volume mixing ratio (VMR) in parts per million (ppm) and total columns and partial columns in molecules per centimetre squared (molec/cm^2). Other variables include altitude, date/time, pressure, a priori vertical profile, averaging kernel matrix and retrieval uncertainties, both systematic and random. The random uncertainties are determined from the temperature, solar zenith angle, and measurement noise from the signal-to-noise ratio. Systematic uncertainties are determined from temperature and line parameters such as line strength and width.

The averaging kernel matrix represents the relationship between the retrieved state and the true atmospheric state at each altitude layer and the sensitivity of a retrieval is calculated by taking the sum of the rows of the averaging kernel. This indicates how much of the information is coming from the a priori profile, and how much comes from the measurement itself (Rodgers, 2003; Vigouroux et al., 2009). The degrees of freedom for signal (DOFS) is calculated by taking the trace of the averaging kernel; this indicates the number of independent pieces of information coming from each retrieval, or inversely, the number of components not constrained by the a priori. The random and systematic FTIR partial column uncertainties are calculated using the error covariance matrices, following the method outlined in Vigouroux et al. (2009). The square root of the associated error is taken, and this is scaled to a percent uncertainty using the corresponding partial column sum. The mean systematic and random percent errors are added in quadrature to get the overall mean percent uncertainty for the species. The number of measurements, mean DOFS, and mean percent uncertainty of the 0-7 km partial columns of CH_4, CO, and O_3 for 2008, 2009, 2014, and 2015, for each station, are listed in Table 2. The mean partial column (0-7 km and 7-20 km) and total column averaging kernels for CH_4, CO, and O_3 for 2008, 2009, 2014, and 2015, are shown in Fig. 1. The lowest level difference between Kiruna, and the other locations results from the use of a stronger constraint for the lowest level with the PROFFIT retrieval, however, retrieval error and noise deem the agreement between the AVKs reasonable (Hase et al., 2004). The DOFS and averaging kernels are indicators of the vertical information within a retrieval. Fig. 1 shows the mean partial column averaging kernels for 0-7 km and 7-20 km are distinguishable, with maxima at different altitudes. The mean total column averaging kernels for all three species appear smooth around 1.0, which indicates that contributions from all altitudes have

Deleted: error

Deleted: The plot is focused on the 0-7 km column

similar weights in the total column. By altitude, the sensitivity of each species is >0.5 in the partial column examined (not shown), meaning that more than half of the retrieved profile information comes from the measurement (Vigouroux et al., 2009). The average DOFS vary by species and station, given the reduced column height of 0-7 km, some of the values are less than one, meaning the retrieval is somewhat constrained by the a priori. However, it should be noted the comparisons presented in this paper account for the vertical sensitivity of the FTIR measurements by smoothing the model data with the averaging kernels. This process is described in Sect. 3.

Deleted: is well defined at those levels

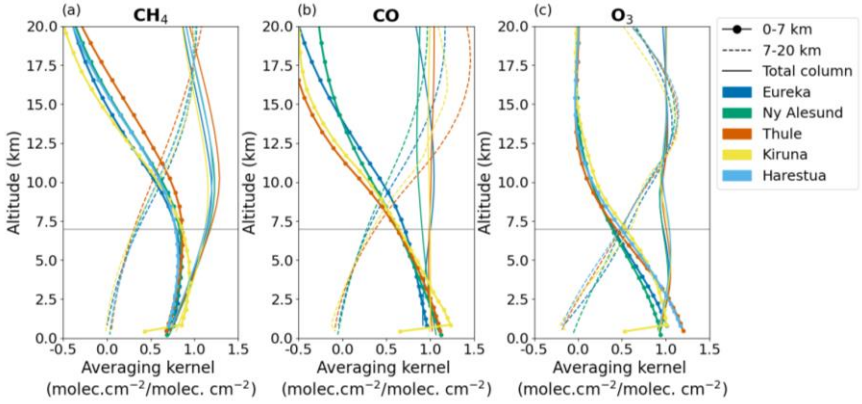

Figure 1: Mean 0-7 km partial column averaging kernelx (linex with circle markers), mean 7-20 km partial column averaging kernels (dashed lines), and mean total column averaging kernels (solid lines), all in units of (molec/cm^2)/(molec/cm^2), by altitude, for (a) CH_4, (b) CO, and (c) O_3. Means are for 2008, 2009, 2014, and 2015 for all five FTIR sites except Harestua (no 2008 data).

Table 2: Summary of FTIR measurement statistics.

Site	Number of Measurements (2008, 2009, 2014, 2015)			Mean DOFS (0-7 km)			Mean Percent Uncertainty (0-7 km)		
	CH_4	CO	O_3	CH_4	CO	O_3	CH_4	CO	O_3
Eureka	754	736	684	0.84	1.1	0.80	4.6	3.9	8.2
Ny Ålesund	205	128	121	0.81	1.3	0.79	11.5	7.7	4.9
Thule	406	459	474	0.78	1.6	1.2	5.7	5.4	3.9

Deleted: Error

Kiruna	397	299	322	0.96	1.6	0.86	3.6	6.4	7.2
Harestua	151 (no 2008)	No CO	169 (no 2008)	0.78	N/A	1.12	5.2	N/A	4.1

Deleted: 93

Deleted: 81

2.2 Atmospheric models

The models used in this study provide three-dimensional VMR fields on 3-hourly intervals for 2008, 2009, 2014, and 2015. These four years were selected for the 2021 AMAP SLCF Assessment; 2008 and 2009 were previously evaluated in the 2015 AMAP Report and 2014 and 2015 were added to include more recent results from years for which Arctic measurements were available at the time (AMAP, 2021). The gases CH_4, CO, and O_3 were chosen for this study as model output for these species was available at 3-hourly intervals, and the FTIR measurements have good sensitivity for them throughout the 0-7 km with the FTIR, as discussed in the previous section. Note that not every model has provided all three gases; there are three which have CH_4, nine with CO, and 11 with O_3 (see Table 3). The model simulations are the same as those discussed in Whaley et al. 2022, 2023, and the 2021 AMAP SLCF Report, however, the analyses there were performed with the monthly-mean output, while the analysis here is with the 3-hourly output, all of which is available at http://crd-data-donnees-rdc.ec.gc.ca/CCCMA/products/AMAP/. While more models participated in the AMAP SLCF Assessment (18 total) and other species were simulated, these were not included in the current study because either the models did not have 3-hourly outputs or the FTIR retrievals had insufficient tropospheric sensitivity (e.g., NO_2).

Deleted: selected for

This set of models is a mix of Earth system models, chemical transport models, global transport models, and chemistry climate models. The models all used the same set of anthropogenic emissions from ECLIPSE v6b (Evaluating the Climate and Air Quality Impacts of Short-Lived Pollutants) by the IIASA GAINS (International Institute for Applied Systems Analysis – Greenhouse gas – Air pollution Interactions and Synergies) model (Amann et al., 2011; Klimont et al., 2017; Höglund-Isaksson et al., 2020). However, the models differ in their use of biogenic and volcanic emissions, tropospheric gas-phase chemistry complexity, and pressure/spatial grids. Four of the 11 models simulate the stratosphere fully, one (GEOS-Chem) uses a simplified linearized stratospheric chemistry, one (GEM-MACH) only simulates the troposphere and the rest use prescribed climatologies at the stratospheric boundary (Whaley et al., 2022). Nine of the 11 models examined use the Global Fire Emissions Database (GFED, van der Werf et al., 2017) or GFED-based (CMIP6) forest fire emissions, and nine of the 11 exclusively use ECLIPSEv6b for agricultural waste burning. A summary of the models is presented in Table 3, including which gases are included in this study, their resolution, and to what degree stratospheric chemistry is considered. It should be noted that the CH_4 concentrations in these models have been prescribed (Whaley et al., 2022). The prescribed concentrations are input at the bottom model layer, and all come from the same dataset (Prather et al., 2012; Olivié et al., 2021), but the resulting CH_4 partial columns differ based on the processes within each model. For a full description of the models, see Appendix A of Whaley et al. (2022) and the references in Table 3.

Deleted: Note that not every model has provided all three gases. This …

Deleted: a variety

Deleted: different levels of

Deleted: and only some

Deleted: A summary of the models is presented in Table 3.

Table 3: Summary of models used in this study.

Model	3-Hourly Outputs	Primary Reference	Horizontal Resolution / Scale	Stratospheric Chemistry
CESM *Community Earth System Model*	CO, O_3	Liu et al. (2016); Danabasoglu et al. (2020)	1.9° × 2.5° global	comprehensive
CMAM *Canadian Middle Atmosphere Model*	CH_4, CO, O_3	Jonsson et al. (2004); Scinocca et al. (2008)	3.75° × 3.75° global	comprehensive
DEHM *Danish Eulerian Hemispheric Model*	O_3	Christensen (1997); Brandt et al. (2012); Massling et al. (2015)	50 km polar stereographic	none
EMEP MSC-W *European Monitoring and Evaluation System-Meteorological Synthesizing Center - West*	CO, O_3	Simpson et al. (2012, 2019)	0.5° × 0.5° global	prescribed
GEM-MACH *Global Environmental Multiscale Model - Modelling Air Quality and Chemistry*	CO, O_3 (only 2015)	Gong et al. (2015); Makar et al. (2015a,b); Moran et al. (2018)	15 km Arctic regional	none
GEOS-CHEM *Goddard Earth Observing System - Chemistry*	CH_4, CO, O_3	Bey et al. (2001)	2° × 2.5° global	simplified
MATCH *Multi-Scale Atmospheric Transport Chemistry*	CO, O_3	Robertson et al. (1999)	0.75° rotated lat-lon regional	prescribed
MATCH-SALSA *Multi-Scale Atmospheric Transport Chemistry - Sectional Aerosol Module for Large Scale Applications*	CO, O_3	Robertson et al. (1999); Andersson et al. (2007); Kokkola et al. (2008)	0.75° rotated lat-lon regional	prescribed
MRI-ESM2 *Meteorological Research Institute - Earth System Model Version 2*	CH_4, CO, O_3	Kawai et al. (2019); Yukimoto et al. (2019); Oshima et al. (2020)	chemistry: 280 km general: 120 km global	comprehensive
UKESM1 *U.K. Earth System Model Version 1*	O_3	Kuhlbrodt et al. (2018); Williams et al. (2018); Sellar et al. (2019)	140 km global	comprehensive
WRF-CHEM *Weather Research and Forecasting Model with Chemistry*	CO, O_3 (only 2014 / 2015)	Marelle et al. (2017, 2018)	100 km regional-Arctic	prescribed

Deleted: Colour Key

3 Methods

As mentioned, the models provided 3-hourly VMRs on model-specific pressure levels and latitude/longitude grids. The process of aligning the model output to FTIR data is described by the flowchart in Fig. 2.

Deleted: The FTIR data are publicly available on the NDACC data repository [https://www-air.larc.nasa.gov/missions/ndacc/data.html], and the model data are available at http://crd-data-donnees-rdc.ec.gc.ca/CCCMA/products/AMAP/.

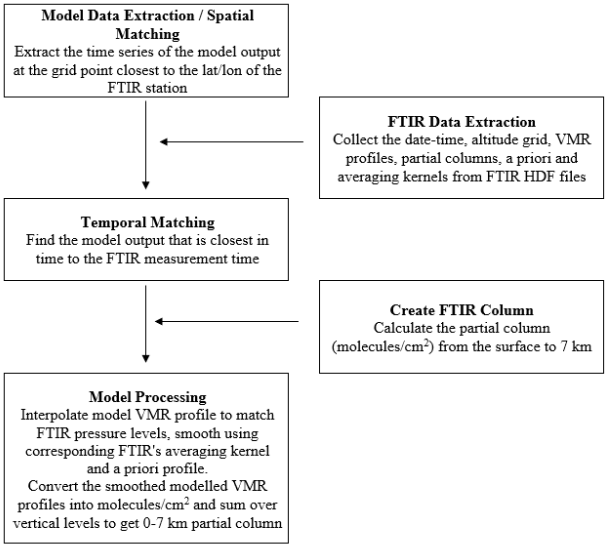

Figure 2: Flow chart depicting the process of matching model output to FTIR data.

This procedure modifies the model output to correspond to an FTIR measurement, making the resulting partial columns equivalent for further comparison. The date/time and volume-mixing-ratio profiles from the model output are extracted from the grid point that is closest to the FTIR location. The FTIR measurements are matched with the 3-hourly model measurement closest in time (±<1.5 hours), this is done to minimize the time difference between the two points, such that no measurement is greater than 1.5 hours from a modelled output. If more than one FTIR measurement coincides with a model output (i.e., multiple measurements are within 1.5 hours of the same model time), the FTIR measurements are averaged. After the model outputs are matched to the FTIR measurements, they are interpolated onto the pressure grid of the FTIR profile. Then, the model VMR profile is smoothed using the respective FTIR measurement's averaging kernel and a priori profile. The purpose of smoothing the model data with the FTIR averaging kernel is to adjust the model to the vertical sensitivity of the FTIR measurement (Rodgers and Connor, 2003). The calculation for the smoothing is shown in Eq. 1, where $\boldsymbol{x_a}$ is the FTIR a

priori VMR vertical profile, **A** is the VMR averaging kernel matrix from the corresponding FTIR measurement, and $\boldsymbol{x}_{model}$ is the modelled VMR vertical profile:

$$\boldsymbol{x}_{smooth} = \boldsymbol{x}_a + \boldsymbol{A} \times [\boldsymbol{x}_{model} - \boldsymbol{x}_a] \,. \quad (1)$$

The model VMR profile is then transformed to a layer profile in units of molecules per centimeter squared using the ratio between the VMR and layer partial column (in molecules per centimeter squared) in the retrieved FTIR profile as the conversion factor. At this point, the model output has the same altitude grid and units as the FTIR retrieval, which allows for partial columns to be summed. Partial columns from 0-7 km were calculated given AMAP's focus on SLCFs in the troposphere, with the cap at 7 km chosen to limit any stratospheric influence. Note that "0 km" is used as proxy for the minimum altitude, but this varies, based on location, with the altitude of each instrument listed in Table 1. The partial column examined here (0-7 km) encompasses 11 vertical layers for all sites, except Ny Ålesund, which has an additional (12th) layer given the lower altitude of its location (see Table 1).

To compare the model and FTIR partial columns, a model-measurement percent difference (Δ_i) is calculated, as defined by Eq. 2 for a single model-measurement pair (i), where $PC_{M,i}$ and $PC_{F,i}$ are the 0-7 km partial columns for the model and FTIR, respectively:

$$\Delta_i = \left(\frac{PC_{M,i} - PC_{F,i}}{PC_{F,i}}\right) \times 100 \,. \quad (2)$$

A regression line is fit to the raw scatter-plot data of the model output versus FTIR measurements using all the available data points, where each plot includes the equation of this line and the correlation coefficient, R^2. The normalized root mean square error (NRMSE), given by Eq. 3, is presented for each model and location, where N is the total number of model-measurement pairs (Kärnä and Baptista, 2016). The root mean square error is normalized to the standard deviation of the FTIR data (σ_F) used in the respective analysis:

$$NRMSE = \frac{1}{\sigma_F}\sqrt{\left[\sum_{i=1}^{N}(PC_{M,i} - PC_{F,i})^2\right]} \,. \quad (3)$$

In addition to evaluating the models using every available FTIR data point in the analysis years, the monthly mean annual cycles are also presented. The monthly mean partial columns ($PC_{F,monthly,j}$) are calculated by taking the mean of every measurement in a given month (j), where N_j is the number of points included in the month for all years considered. The monthly model mean partial columns ($PC_{M,monthly,j}$) are made in the same manner, using only the smoothed partial columns that have a corresponding matching FTIR measurement, as defined above. Equation 4 outlines the calculation of a monthly mean partial column for month j for a: the FTIRs ($PC_{F,monthly,j}$), and b: the models ($PC_{M,monthly,j}$):

$$PC_{M,monthly,j} = \frac{1}{N_j}\sum_{i=1}^{Nj} PC_{M,i}. \quad (4a)$$

$$PC_{F,monthly,j} = \frac{1}{N_j}\sum_{i=1}^{Nj} PC_{F,i}. \quad (4b)$$

Deleted: column

Deleted: C_m and C_F

Deleted: lists

Deleted: , is calculated based on the line of best fi of the model results versus FTIR measurements using all the available data points

Deleted: percent

Deleted: percent

Deleted: in

Deleted: .

Deleted: ($N_{m,j}$), for 2008, 2009, 2014, and 2015

The model-measurement monthly mean percent difference ($\Delta_{monthly,j}$), shown by Eq. 5, follows the same process as the monthly-mean partial column, and is the mean value from Eq. 2 for each month (j) across the years, where the error bars on the monthly mean plots represent the standard deviation of this mean:

$$\Delta_{monthly,j} = \frac{1}{N_j}\sum_{i=1}^{Nj} \Delta_i. \quad (5)$$

The mean of these monthly mean differences is used to calculate the overall mean percent difference (Δ_O) for each model, sometimes referred to as model bias, where N_{months} is the number of measurement months in a calendar year at that location (see Table 1), and the uncertainty given is the standard deviation of this mean:

$$\Delta_O = \frac{1}{N_{months}}\sum_{j=1}^{N_{months}} \Delta_{monthly,j}. \quad (6)$$

Finally, the monthly multi-model mean (MMM) partial column for month j ($PC_{MMM,monthly,j}$) is calculated by taking the mean $PC_{M,monthly,j}$ for all models, at a given location, calculated with Eq. 4b, and the MMM monthly mean difference ($\Delta_{MMM,monthly,j}$) is the mean of $\Delta_{monthly,j}$ for all models, at a given location calculated with Eq. 5. The overall percent difference of the MMM-measurement ($\Delta_{O,MMM}$) is given by Eq. 7:

$$\Delta_{O,MMM} = \frac{1}{N_{months}}\sum_{j=1}^{N_{months}} \Delta_{MMM,monthly,j}. \quad (7)$$

These steps are taken to establish the modelled seasonal cycles, and quantify the differences between the models and measurements, by month and season. Further, assessing the MMM by month allows for a general overview of when and where models diverge from measurements and can help suggest shortcomings in the models. There are not enough measurements per day to evaluate a diurnal cycle, although it is expected to be small in the Arctic, and there are not enough years available in the 3-hourly dataset used here to examine long-term trends.

When discussing FTIR uncertainty, this refers to the mean uncertainty per gas and station, as listed in Table 2. When discussing the mean difference between the model and measurements, this refers to the overall mean difference (Δ_O) as described by Eq. 6. In Sects. 4 and 5, these two parameters are used to assess model performance: if Δ_O is within measurement (FTIR) uncertainty, the model can be considered in general agreement with the FTIR; if $\Delta_O \pm$ the standard deviation of the mean is within the measurement uncertainty, then the model is sometimes in agreement with the measurements; and if the uncertainty and Δ_O do not overlap then the model and measurements do not agree.

4 Results and discussion

This section presents the analyses described above, for CH_4, CO and O_3, and discusses the findings in the context of the 2021 AMAP SLCF Assessment Report, and other related literature. Given the volume of data (three species, five locations, and 11 models), only selected plots are shown in the main text, with the remaining figures provided in Appendices A-C. In the appendix there are plots for each location, showing the time series of the 0-7 km partial column for each measurement / model pair and the associated model-measurement percent difference, the equivalent plot reduced to monthly mean data (an

individualized version of Figs. 3, 5 and 9), and the 0-7 km column of FTIR vs smoothed model for the remaining locations (analogous to Figs. 4, 8 and 10). Table 4 provides a summary of the overall differences for each model and location by species, as described by Eq. 6. Table 5 summarizes the overall MMM difference for each species at each location, and the overall average for each species. All the comparisons shown are for a 0-7 km partial column, where the model output is smoothed as described by Eq. 1.

4.1 CH_4

CH_4 is a powerful greenhouse gas (GHG) after CO_2, and its emissions are expected to increase in the Arctic due to melting permafrost (IPCC, 2021). CH_4 is also involved in the formation of tropospheric O_3, which is the third strongest anthropogenic GHG and an air pollutant at the surface. Therefore, it is important for both air quality and climate models to represent CH_4 accurately. The CH_4 plots for Ny Ålesund, Thule, Kiruna, and Harestua are provided in Appendix A, following the same order discussed here for Eureka.

Figure 3 shows the monthly mean 0-7 km partial column time series for the FTIR and models at each location (a-e), with the percent difference between the monthly mean model and monthly mean measurement for all locations shown in panel f. This shows that apart from a few outliers, the pattern of the seasonal cycle of CH_4 is consistent, although the amplitude is underestimated. The uniformity between the years (see A1-A5 for full data timeseries plots) and consistency of the model biases between sites is likely a consequence of CH_4 being prescribed in the models, in addition to the longer lifetime of CH_4, relative to the other SLCFs. This is also seen in Fig. 4 (and Figs. A11-A14), where the model and FTIR columns are compared, with the line of best fit and R^2 are indicated in the legend.

Deleted: . The results from Eureka, Canada are shown in the main text as this location is at the highest latitude and has the most measurement points for all species.

Deleted: the second most important

Deleted: ¶
It should be noted that the CH_4 concentrations in these models have been prescribed and only three of the 11 participating models provided 3-hourly CH_4 concentrations (Whaley et al., 2022). The prescribed concentrations are input at the bottom model layer and all come from the same dataset (Prather et al., 2012; Olivié et al., 2021), but the resulting CH_4 concentrations differ based on the processes within each model.

Deleted: Eureka

Deleted: (a) the partial columns and (b)

Deleted: Figure 3 (and Figs. A1-A4)

Deleted: the models simulate a consistent seasonal cycle from year to year for each model/location, with little variance,

Deleted: . Figure 4 (and Figs. A5-A8) shows the monthly means of all the years combined; broadly,

Deleted:

Deleted: seen in the comparisons

Deleted: the longer lifetime of CH_4, relative to the other SLCFs

Deleted: being prescribed in the models

Deleted: 5

Deleted: A9

Deleted: A12

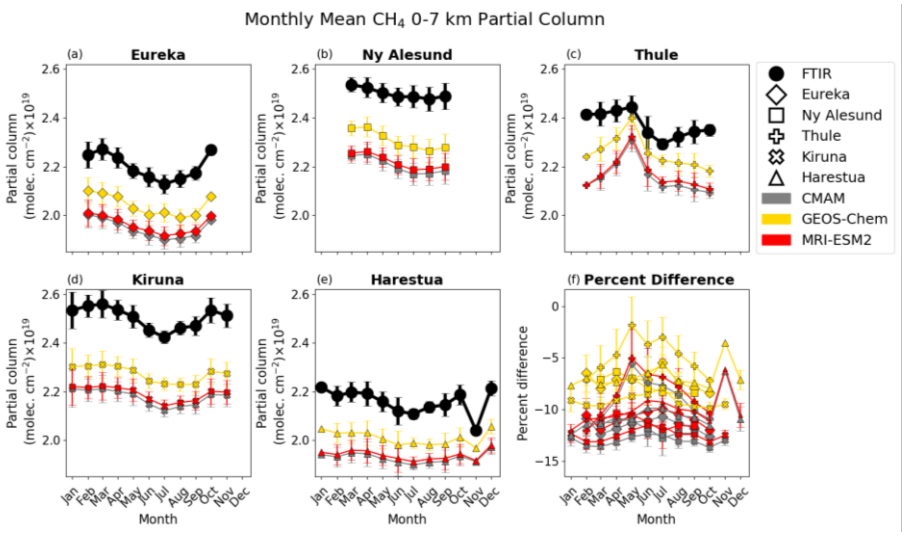

Figure 3: (a-e) Monthly mean FTIR (black) and smoothed model (colour) 0-7 km partial columns of CH_4 ($PC_{F,monthly,j}$ and $PC_{M,monthly,j}$, respectively), for each location, shown with the same y-axis. Error bars represent the standard deviation of the monthly mean. (f) Mean model-measurement percent difference by month ($\Delta_{monthly,j}$) for each model (by colour) and location (by marker). Error bars represent the standard deviation of the monthly mean percent difference.

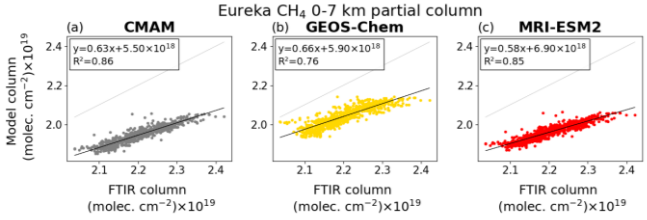

Figure 4: Smoothed model vs. FTIR 0-7 km partial columns of CH_4 for Eureka, showing all available model-FTIR corresponding data. The black line is the line of best fit, where the equation and R^2 are noted in the legend. The 1:1 line is shown in light grey.

Deleted: 4

Deleted: led

Deleted: ng model data that are the nearest in time to each FTIR measurement shown in Figure 3.

Deleted: b

Deleted: The legend on panel (b) shows the overall mean percent difference and its standard deviation.

Deleted: 5

Deleted: M

A summary of the overall mean difference, R^2, and the normalized root-mean-square error for each location is shown in Fig. 5. Across all three models, Arctic CH_4 is underpredicted compared to the FTIR measurements. The surface in situ CH_4 comparison in Whaley et al. (2022) showed that measured surface CH_4 VMRs are much more variable than the modelled VMRs. However, in the 0-7 km partial columns in this study, CH_4 is well-mixed and more homogenous, resulting in better agreement between the models and the FTIR measurements. The low bias we find in this study for the Arctic sites is consistent with the global comparisons of these models to satellite measurements in Whaley et al. (2022), which found that some models did not distribute CH_4 with an accurate north-south gradient, resulting in low biases in the Arctic and high biases in lower latitudes. GEOS-Chem does simulate a north-south gradient, which is reflected in the smaller overall model-measurement percent difference, compared to other models, in all locations (note Fig. 6 in Whaley et al., 2022). However, the R^2 of GEOS-Chem vs. FTIR is smaller than that for the other models at some locations (Eureka and Kiruna), which can be attributed to the increase in variability the gradient introduces – including some instances of overestimation. The mean differences for each model across sites are relatively consistent, while the results vary more when comparing R^2 and NRMSE. Particularly, when comparing between the same model, the R^2 for Ny Ålesund is the lowest and the NRMSE is the highest. The data from Ny Ålesund show less of a seasonal cycle than the other locations, and the FTIR uncertainty for CH_4 at Ny Ålesund is more than twice that of the other sites (see Table 4). The larger uncertainty may lead to reduced sensitivity to small changes, and increased variability masking seasonal changes, which can contribute to the discrepancy between the models and observations. The mean difference for GEOS-Chem is within the uncertainty of the FTIR measurements for Ny Ålesund, and Thule, as is the mean difference for MRI-ESM2 at Ny Ålesund, none of the other models are within the FTIR uncertainty at the given location (see Table 4).

Deleted: 6

Deleted: Eureka, Thule, and Kiruna all have R^2 values nearest to 1 across the models, and these sites also have the largest number of CH_4 measurements. For all models, the R^2 values for Ny Ålesund and Harestua are significantly smaller, while the overall mean percent difference (Δ_O) is comparable to the other locations. The discrepancy is likely attributed to the smaller number of measurement points, causing outliers to have more weight in the linear regression, which is reflected in the elevated NRMSE for Ny Ålesund across all models.

Deleted: This shows that the models can represent the temporal variability well, despite low biases in magnitude.

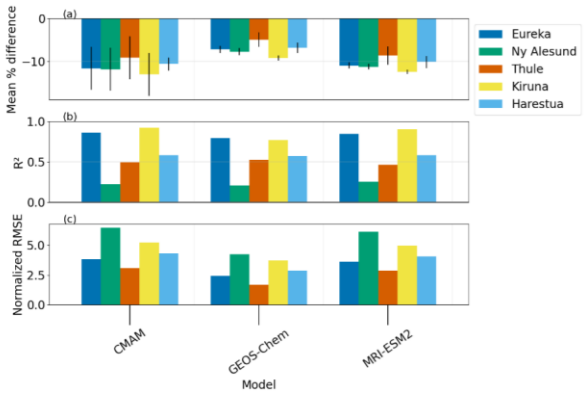

Figure 5: By model and location: (a) Overall model-measurement mean percent difference for CH_4 0-7 km partial columns (Δ_o), with error bars that represent the standard deviation of the mean, as shown in the legend of Figs. A6-A10. (b) R^2 as shown in Figs. 4 and A11-A14. (c) Normalized root-mean-square error.

Figure 6 shows the multi-model mean (MMM) for each location, and the percent difference compared to the monthly mean FTIR. The error bars and shading represent the standard deviation of the mean. The AMAP SLCF Assessment Report compares the models with surface CH_4 measurements and finds that the MMM bias for Arctic CH_4 is +1.3% (AMAP, 2021). When comparing with 0-7 km FTIR partial columns, the MMM bias ranges from -5 to -15% (Fig. 6(f)) and unlike the results in the AMAP Report, the comparisons are not improved by choosing a multi-model mean because all three models have a negative bias. The FTIR retrievals show good sensitivity to tropospheric CH_4 (sensitivity >0.5), however, as these column measurements average out CH_4 biases over the tropospheric column, they are not expected to exactly match the surface measurement comparisons. Furthermore, due to the sharp decrease in CH_4 above the tropopause (Whaley et al., 2022), a poor representation of the tropopause height may contribute to the low bias in the modelled 0-7 km partial columns, as shown from O_3 data in Whaley et al., 2023. The AMAP Report also includes a comparison with upper-troposphere/lower-stratosphere (UTLS) CH_4 VMRs as measured by the ACE-FTS (Atmospheric Chemistry Experiment - Fourier Transform Spectrometer) satellite instrument and finds that the models are biased low by ~100 ppbv in the vicinity of the tropopause (300hPa; around~8-9km), indicating that the modelled tropopause may be too low (Whaley et al., 2022). The results found here are consistent with Whaley et al. (2022), in that that the model simulations of both the lower troposphere (0-7 km partial columns) and the UTLS are biased low, and models with north-south CH_4 gradients (here, only GEOS-Chem) have smaller biases than those that do not. Generally, the models can represent the temporal variability in the tropospheric column well, although are biased low in magnitude, outside of the range of the FTIR uncertainty.

Deleted: 6
Deleted: 4b, and
Deleted: 5
Deleted: A8
Deleted: 5
Deleted: 9
Deleted: 2
Deleted: 7
Deleted: 7
Deleted: to surfac
Deleted: e
Deleted: This is consistent with the results found here, suggesting
Deleted: This shows that
Deleted: despite low biases

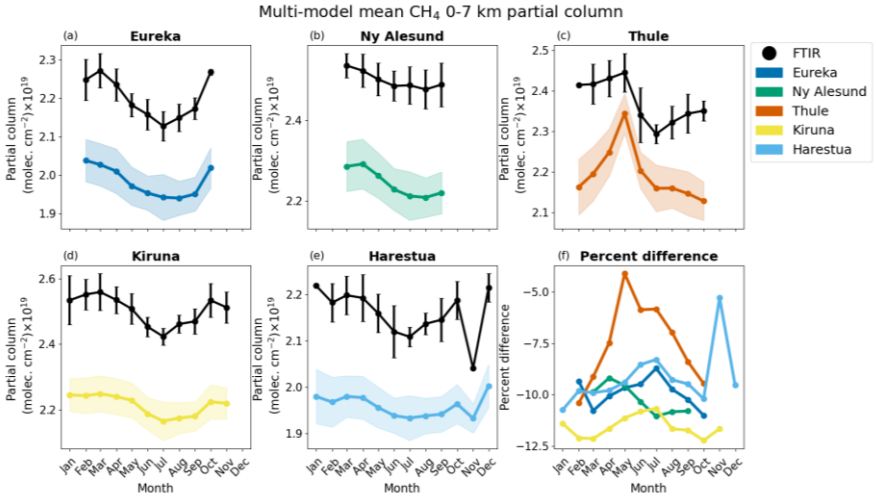

Figure 6: (a-e) Monthly mean FTIR (black) and multi-model mean (coloured) 0-7 km partial columns of CH_4 ($PC_{F,monthly,j}$ and $PC_{MMM,monthly,j}$, respectively), with error bars and shaded areas, respectively, representing the standard deviation of the mean. (f) Monthly mean percent difference of the MMM ($\Delta_{O,MMM}$) for all locations.

Deleted: 7

4.2 CO

Like CH_4, CO is involved in tropospheric O_3 formation in the presence of NO_x. Thus, in order to properly simulate tropospheric O_3, it is important for models to accurately simulate CO. In the Arctic, CO is used as a tracer for identifying and quantifying influences from biomass burning and lower latitude anthropogenic emissions (e.g., Fisher et al., 2010; Monks et al., 2015; Viatte et al., 2015; Lutsch et al., 2020)

Nine of the 11 models examined in this study provided 3-hourly outputs for CO; WRF-Chem only has outputs for 2014 and 2015, and GEM-MACH only has data for 2015 (Table 3). Seven of the nine CO models examined use GFED-based fire emissions. The remaining models are EMEP MSC-W which uses FINN fire emissions and GEM-MACH which uses CFFEPS fire emissions (Whaley et al., 2022). Evidence of biomass burning events can be observed in the summer months when examining the CO seasonal cycle with all available measurement points, where there are sporadic increases in the measured CO (Figs. B1-B4). The CO timeseries data (i.e. Figs. B1-B4 and 7 /B5-B8) indicates that the GFED-based models may overestimate CO from biomass burning as their bias shifts positive in the summertime relative to the rest of the timeseries.

Deleted: The results for CO at Eureka are provided below with Ny Ålesund, Thule, and Kiruna results provided in Appendix B. Figure 8 (and Figs. B1-B3) shows the CO seasonal cycle with all available measurement points;

Deleted: e

Deleted: where

Deleted: Seven of the nine CO models examined use GFED-based fire emissions. The remaining models are EMEP MSC-W which uses FINN fire emissions and GEM-MACH which uses CFFEPS fire emissions (Whaley et al., 2022).

Deleted: T

This feature is absent for GEM-MACH which does not have a consistent trend between sites during the summer (although results are only available for one year), and for EMEP MSC-W which shifts more negatively in the summertime. It is well known that the fire emissions inventories vary greatly from each other (AMAP, 2021), causing these differences in model results.

Figure 7 (and Figs. B5-B8) shows the monthly mean partial columns and percent differences between the models and the FTIR measurements. This allows for an overview of the mean percent difference and how the model biases change over the year. For example, MATCH exhibits a positive shift in bias from the end of summer to the fall in all locations. WRF-Chem is biased low in the spring and summer, but agrees better with the observations from August onwards, in contrast to EMEP-MSC-W, which tends to diverge from the measurements in the mid- to late summer. GEM-MACH is the only model that has a positive mean difference in all locations. The year-round difference is likely due to the fact that this model used anthropogenic emissions produced locally for most of its regional domain, instead of the ECLIPSEv6B anthropogenic emissions that all of the other models used, and lateral regional boundary conditions provided from MOZART4 (Model for Ozone and Related Chemical Tracers, version 4) global simulations (Emmons et al., 2010; Gong et al., 2018; AMAP, 2021). Further, Fig. 8 (and Figs. B9-B11) shows the correlations between the modelled and FTIR partial columns, with the line of best fit and R^2 indicated in the legend. For many models, the 1:1 correlation (and Figs. 8, B9-B11) shows that models have better agreement with the FTIR for low CO values and the disparity increases as CO increases, i.e. the line of best fit and 1:1 line diverge. The points with the maximum CO VMRs correspond to the FTIR springtime peak in the CO cycle (since wintertime CO measurements are not possible during polar night).

Deleted: 9
Deleted: B4
Deleted: 6
Deleted: s
Deleted: (a)
Deleted: (b)
Deleted: 10
Deleted: B7
Deleted: 9
Deleted: comparison of
Deleted: comparison
Deleted: 10
Deleted: B7
Deleted: 9

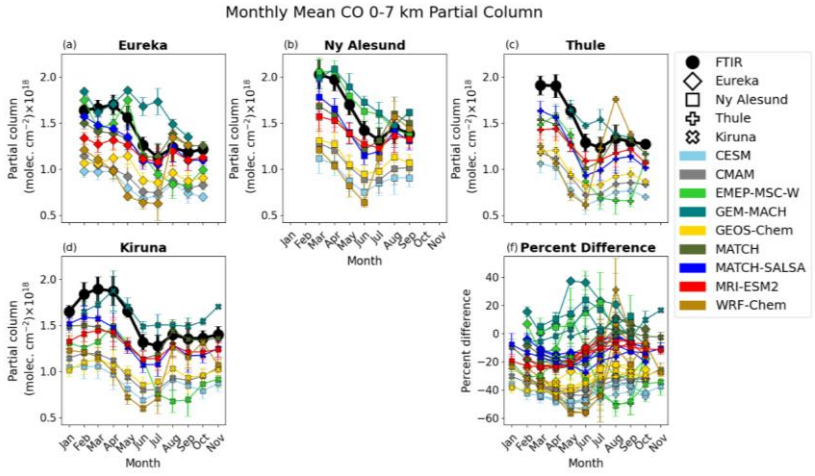

Figure 7: (a-e) Monthly mean FTIR (black) and smoothed model (colour) 0-7 km partial columns of CO ($PC_{F,monthly,j}$ and $PC_{M,monthly,j}$, respectively), for each location, shown with the same y-axis. Error bars represent the standard deviation of the monthly mean. (f) Model-measurement mean percent difference by month ($\Delta_{monthly,j}$) for each model (by colour) and location (by marker). Error bars represent standard deviation of the monthly mean percent difference.

Deleted: 9

Deleted: Monthly mean FTIR (black) and modelled (colour) partial columns of CO, from Eureka using model data that are the nearest in time to each FTIR measurement shown in Figure 8. Error bars represent the standard deviation of the monthly mean. (b) Mean percent difference by month. Error bars represent standard deviation of the monthly mean percent difference. The legend on panel (b) shows the overall mean percent difference and its standard deviation

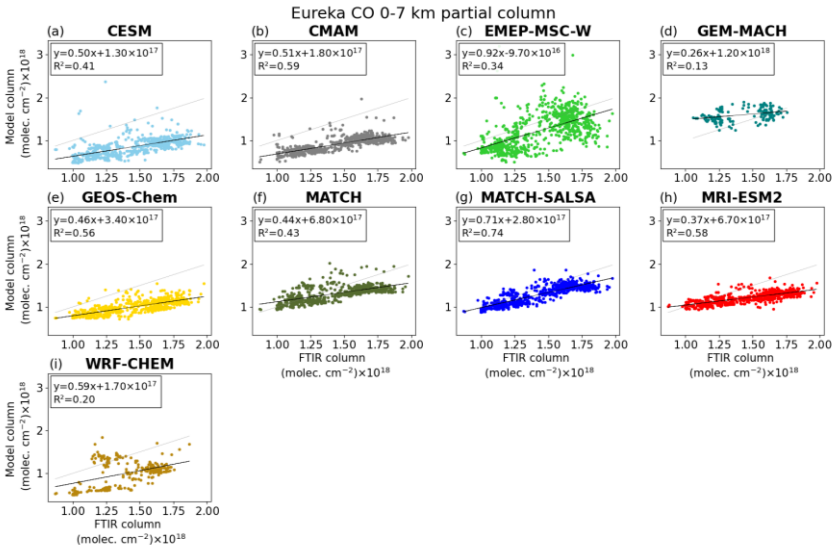

Figure 8: Smoothed model vs. FTIR 0-7 km partial column of CO for Eureka, showing all available model-FTIR corresponding data. The black line is the line of best fit, where the equation and R^2 are noted in the legend. The 1:1 line is shown in light grey.

Figure 9 summarizes the overall model-measurement mean percent difference R^2, and normalized root-mean-square error for all locations. GEM-MACH has a mean percent difference that is within the FTIR uncertainty for Thule and Kiruna, EMEP MSC-W and MATCH are simulated within the mean FTIR uncertainty for Ny Ålesund (see Table 4). MATCH-SALSA and MRI-ESM2 exhibit high R^2 and low percent difference across all locations, relative to the other models' values, although their columns do not fall within the FTIR uncertainties. GEM-MACH and MATCH have NRMSE comparable to MATCH-SALSA and MRI-ESM2, despite generally lower R^2. WRF-Chem shows better agreement with the FTIR measurements from Eureka, where the NRMSE is comparable to CESM, CMAM and GEOS-Chem. This is likely a result of the increased density of measurement points in August and September, when WRF-Chem exhibits a minimum bias compared to the FTIR data, and because the comparison only includes data points from 2014 and 2015. The large negative biases earlier in the year lead to low R^2 and high NRMSE at all sites. This appears to be linked to negative biases in modelled surface CO over mid-latitude source regions, and in the free troposphere compared to MOPITT data, as reported by Whaley et al. (2022). Overall, four model-location pairs have a mean difference within the average FTIR 0-7 km partial column uncertainty (see Table 2), and when including the standard deviation of the mean difference, an additional eight pairs out of 36 meet this criterion.

Deleted: 10
Deleted: M
Deleted: 11
Deleted: erro
Deleted: r
Deleted: error
Deleted: average error
Deleted: a
Deleted: comparisons
Deleted: for
Deleted: /

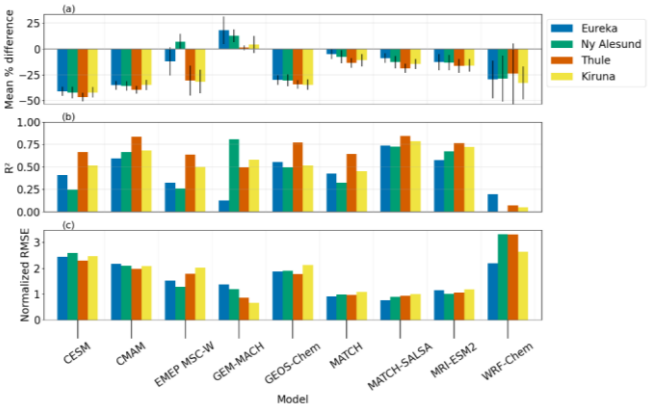

Figure 9: By model and location: (a) Overall model-measurement mean percent difference for CO 0-7 km partial columns (Δ_O), with error bars that represent the standard deviation of the mean, as shown in the legend of Figs. B5-B8. (b) R^2 as shown in Figs. 8 and B9-B11, (c) Normalized root-mean-square error.

Deleted: 11

Deleted: 9b andB6

Deleted: 10

Deleted: 7-9

Figure 10 shows the monthly MMM for CO at each location, with the percent difference in the last panel (f). This highlights the general tendency of the models to underpredict tropospheric CO more in the spring than in the summer, which has been observed by other Arctic model-measurement comparison studies. The AMAP SLCF Assessment Report found that compared to CO from various surface networks, the models had a greater bias than for the other SLFCs examined, underestimating CO in the spring and overestimating CO in the summer (AMAP 2021). The same pattern was observed when comparing with MOPITT (Measurements of Pollution In The Troposphere) satellite CO in the free troposphere, at the 600 hPa level (Whaley et al., 2022). The change from a negative winter-spring bias to a positive summer bias was observed in model comparisons to surface CO measurements at two additional Arctic sites, Zeppelin, Norway and Utqiagvik/Barrow, USA , with a -20-30% bias in the first six months of the year (Whaley et al., 2023), which is compatible with results shown in Fig.10(e).

Deleted: 12

Deleted: . Similar trends have

Deleted: found

Deleted: in

Deleted: 6

In POLMIP, models were run for 2008 with a standardized emissions inventory; there is some overlap of models examined here, although a different emissions input was used (see Emmons et al., 2015 for full project description). Similar to the results presented here, the POLMIP study found that relative to surface, airborne, and satellite Arctic tropospheric measurements, CO was underpredicted by the models (MMM gross error 9-12%), with a more negative bias in the winter/spring compared to the summer, although the models still broadly captured the seasonal cycle (Monks et al., 2015). Using an idealized tracer, POLMIP examined anthropogenic and biomass burning influences in Arctic regions, demonstrating a seasonal dependence of transport efficiency. It was shown that for anthropogenic emissions, Europe influences the surface CO, while Asia and North America have more influence higher in the troposphere (Monks et al., 2015). Further more, the tracer

Deleted: The POLARCAT (Polar Study using Aircraft, Remote Sensing, Surface Measurements and Models, of Climate, Chemistry, Aerosols and Transport) Model Intercomparison Project (POLMIP) examined 11 atmospheric models in relation to a variety of Arctic observations taken in 2008 (Emmons et al., 2015).

Deleted: at study

investigation in that study showed that OH differences account for more variability between the models than the transport mechanisms within the individual models. However, it can be noted that although models may reduce negative biases through better OH chemistry, this alone will not resolve the differences between the model and measurements (Monks et al., 2015).

The current study, the POLMIP study, and the AMAP Report exhibit similarities in the model-measurement comparisons of CO, most notably, all three studies show negative biases early in the year, which shift positively in the summer; the model-FTIR comparisons become less negative, while the AMAP-surface measurement comparisons change to a positive bias. Lutsch et al. (2020) also reported a low bias in GEOS-Chem lower tropospheric CO columns compared with measurements from 10 FTIR stations, including four sites in this study, although they found a greater underestimation for Eureka and Thule in July and August due to transported boreal wildfire emissions not fully captured by the model, particularly for years after 2015 not included in the present study. Previously published studies point to underestimated anthropogenic emissions as a source of the discrepancies (Monks et al., 2015, Whaley et al., 2022; 2023). The results of the model-FTIR comparisons presented here support this reasoning, as the only model with a positive bias (GEM-MACH) has additional local Arctic emissions (Gong et al, 2018). The models may be improved with more refined OH chemistry, although it is unlikely to completely resolve the inconsistencies (Monks et al., 2015); improvements to long-range transport and biomass burning inventories could also reduce the differences between model results and measurements.

Deleted: fluxes

Deleted: The results of the model-FTIR comparisons presented here support this reasoning, as the model with a positive bias (GEM-MACH) has a different emissions input, with possibly more complete emissions in the Arctic, as this was a high-resolution Arctic version.

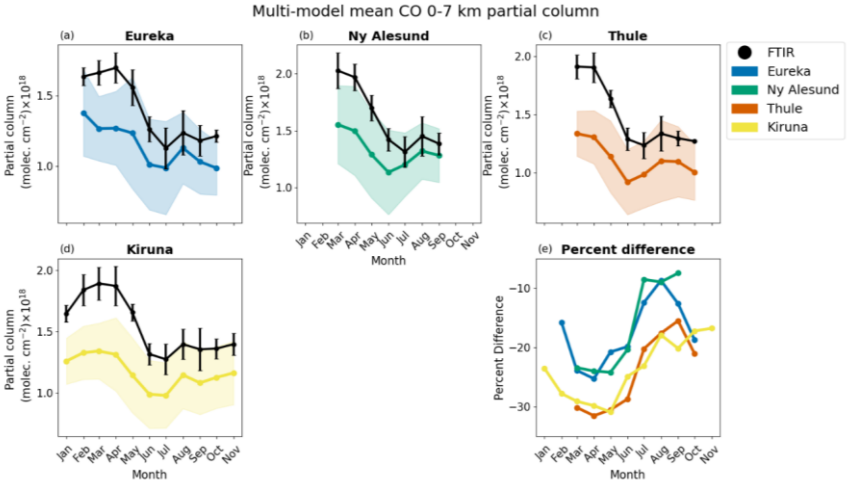

Figure 10: (a-d) Monthly mean FTIR (black) and multi-model mean (coloured) 0-7 km partial columns of CO ($PC_{F,monthly,j}$ and $PC_{MMM,monthly,j}$, respectively), with error bars and shaded areas representing the standard deviation of the mean. (e) Monthly mean percent difference of the MMM ($\Delta_{O,MMM}$) for all locations.

Deleted: 12

4.3 O_3

Tropospheric O_3 is both a significant anthropogenic GHG and an air pollutant that has impacts on human health and ecosystems. In the troposphere, O_3 is a secondary pollutant, produced by photochemical oxidation of volatile organic compounds in the presence of NO_x. In addition to atmospheric photochemistry, its production is highly sensitive to meteorological conditions. Diurnal impacts on O_3 production are minimal in the Arctic, relative to lower latitudes, due to the gradual and prolonged change in solar altitude/angle throughout the year. While O_3 processes are complex, O_3 is often quite well reproduced by models, possibly due to compensating biases in its precursors (Whaley et al., 2022). Although progress has been made, sparse observations, Arctic amplification, and a changing global climate hinder the understanding and modelling of O_3 in Arctic regions (Whaley et al., 2023). For a summary of the current understanding of Arctic tropospheric O_3, see Whaley et al. (2023).

All 11 of the models examined in this study provide 3-hourly O_3 concentrations. The full data timeseries plots (Figs. C1-C5) demonstrate the variation between the models and throughout the year, which is likely a by-product of the complexity in modelling tropospheric O_3. Figure 11 (and Figs. C6-C10) shows the monthly mean partial columns (a-e) and percent differences (f) to highlight the parts of the year which are over or underpredicted. For example, "springtime" (referred to here as when the sun rises, in approximately late February at the highest latitude sites, until May) O_3 is of interest in the Arctic due to the springtime maximum in its seasonal cycle, and the potential for both stratospheric ozone intrusions into the upper (mid) troposphere and surface O_3 depletion events (ODEs) due to bromine explosions and halogen chemistry. However, the 0-7 km partial column FTIR O_3 seasonal cycle, shown here, is dominated by the free troposphere and stratospheric processes, and does not have a springtime minimum from surface ODEs, as one might expect from surface measurements (Solberg et al., 1996; Berg et al., 2003; Skov et al., 2006; Eneroth et al., 2007; Whaley et al, 2023). The Arctic surface ODE features are primarily limited to the near surface/lower boundary layer (<2 km), whereas the 0-7 km partial column is dominated by the free troposphere (Zhao et al., 2016). It can be noted that all of the models in this study lack the necessary halogen chemistry needed to simulate ODEs in the high Arctic (Whaley et al., 2023). Figure 11 shows that across all locations, MATCH-SALSA overpredicts O_3 by 35-75% in winter, which gradually declines until May, after which the bias becomes negative. GEM-MACH, GEOS-Chem, UKESM1 and WRF-Chem underestimate springtime O_3 most substantially across all sites. The discrepancies may arise from inaccuracies in model water vapor leading to an increase in O_3 destruction and/or a lack of O_3 transported from mid-latitudes, which is a substantial source of tropospheric O_3 in the Arctic (Hirdman et al., 2010; Whaley et al., 2023). In the case of the regional GEM-MACH model, low biases in O_3 or precursor species at the lateral boundary conditions may also be contributing. CESM, CMAM, DEHM and MRI-ESM2 demonstrate reasonable agreement with measured springtime O_3 across locations, in addition to a smaller overall mean percent difference, relative to other models. EMEP MSC-W and WRF-Chem simulate springtime O_3 comparable to the aforementioned models, although negative biases later in the year lead to a larger overall mean percent difference. This may indicate that these models have too much photochemical O_3 loss in the summer months.

Deleted: It

Deleted: Therefore, it is difficult for models to accurately

Deleted: simulate tropospheric O_3. Yet,

Deleted: Results for Eureka are shown below and the associated figures for O_3 at Ny Ålesund, Thule, Kiruna, and Harestua are provided in Appendix C. Figure 13 (and Figs. C1-C4) show the entire time series of 0-7 km O_3 partial columns by time of year on panel (a), and the percent difference between the model and FTIR in panel (b). These …

Deleted: 14

Deleted: D5-D8

Deleted: reduce the previous figure(s) to

Deleted: (a)

Deleted: (b)

Deleted: to

Deleted: A

Deleted: and

Deleted: , which

Deleted: be

Deleted: attributed

Deleted: to a low bias in the models' lateral boundary condition,

Deleted:

Deleted: . In the case of the regional GEM-MACH model, low biases in the lateral boundary conditions may also be contributing.

Deleted: and

Figure 12 (and Figs. C11-C14) shows the model versus FTIR O_3 0-7 km partial columns, with the line of best fit and R^2 shown in the legend, along with the 1:1 line. The general underprediction towards the largest values could be related to the underestimation in precursor species (such as CO or NO_x), a lack of long-range transport, an underestimation of ozone production in air masses during long-range transport to the Arctic, or a combination thereof. Using a MOZART-4 tagged tracer simulation of O_3, Wespes et al. (2012) examined source attributions of the tropospheric O_3 columns measured by the FTIR instruments at Thule and Eureka. Their analysis shows that the retrievals have minimal contribution from the a priori (~1%), resulting in high vertical sensitivity throughout the troposphere. The tropospheric column source contributions were estimated, where over half was attributed to anthropogenic sources, followed by stratospheric influence and lastly lightning and biomass burning emissions (Wespes et al., 2012). The seasonal cycle of Arctic O_3 has been shown to vary based on geographical conditions, such as if the site is costal, inland or at a high elevation (Whaley et al., 2023). Moreover, O_3 partial columns can be variable because they depend on the vertical distribution of O_3, which is determined by a combination of emissions, chemistry, dynamics, and radiation, all of which vary with altitude (Rap et al., 2015). Notably, Arctic O_3 columns have strong gradients in the influences on the vertical profile from mid-latitude regions (Europe, North America and Asia), which also vary with season (Monks et al., 2015). The combination of these factors leads to an increasingly complex series of model processes, which can also result in compounding errors. Without sensitivity simulations, like those carried out in Monks et al. (2015) and Rap et al. (2015), it is difficult to definitively say which of these processes are responsible for the underestimations found in this study.

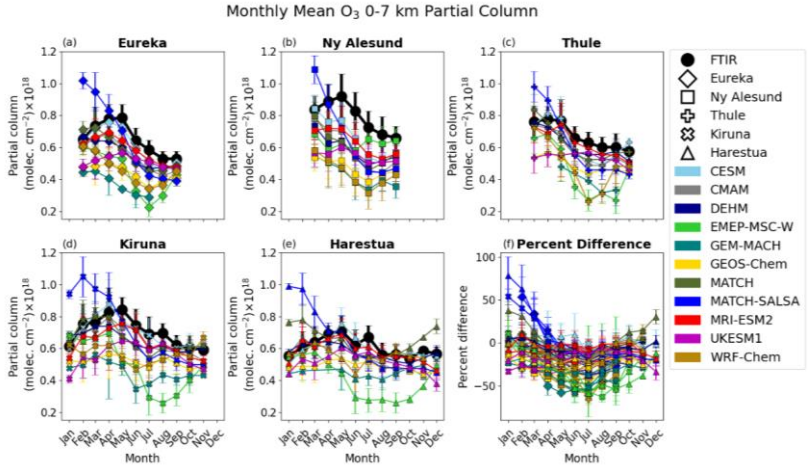

Figure 11: (a-e) Monthly mean FTIR (black) and smoothed model (colour) 0-7 km partial columns of O_3 ($PC_{F,monthly\,j}$ and $PC_{M,monthly\,j}$, respectively), for each location, shown with the same y-axis. Error bars represent the standard deviation of the monthly mean. (f) Model-measurement mean percent difference by month ($\Delta_{monthly\,j}$) for

Deleted: 15
Deleted: 9
Deleted: 2
Deleted: As with CO, many of the models have a better agreement for smaller O_3 partial columns and fail to capture larger values. This
Deleted: difficult to
Deleted: , and as such is recommended for future work.
Deleted: 14

each model (by colour) and location (by marker). Error bars represent standard deviation of the monthly mean percent difference.

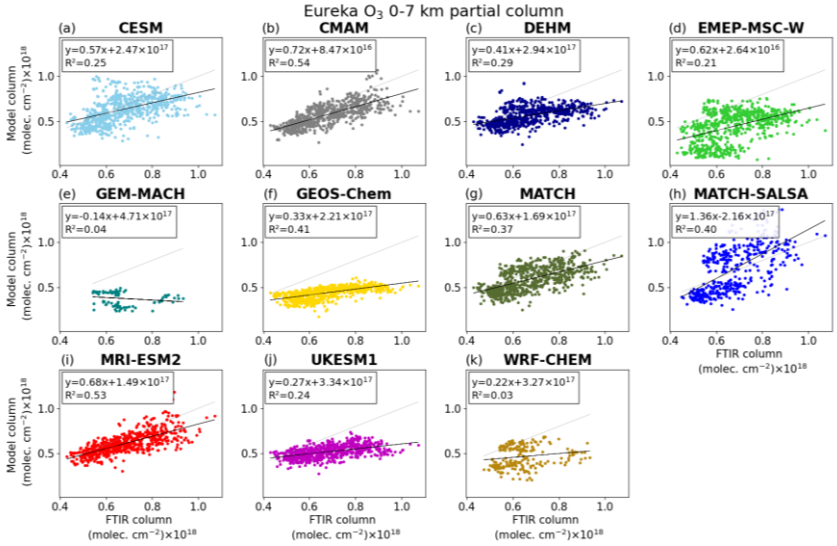

Figure 12: Smoothed model vs. FTIR 0-7 km partial columns of O_3 for Eureka, showing all available model-FTIR corresponding data. The black line is the line of best fit, where the equation and R^2 are noted in the legend. The 1:1 line is shown in light grey.

Figure 13 shows the summary of O_3 mean percent differences, R^2, and normalized root-mean-square error. The model-FTIR comparisons reveal that the spatial resolution, and inclusion of stratospheric chemistry in the models does not necessarily improve results (refer to Table 3 for horizontal resolution and stratospheric chemistry). For example, WRF-Chem, EMEP MSC-W, and GEM-MACH show a low R^2 and higher NRMSE (varying between sites and models), although contributing to this for WRF-Chem and GEM-MACH could be the limited number of analysis years (two and one, respectively). These air-quality focused models have detailed chemistry and were run at higher spatial resolutions, whereas for example CMAM, a climate-focused model, has a coarser resolution with simplified tropospheric chemistry and demonstrates larger R^2 and smaller mean percent differences (Fig. 13). However, when considering the stratosphere, CMAM, which includes comprehensive stratospheric chemistry, has comparable metrics in Fig. 13 to DEHM, which uses prescribed climatologies for the stratosphere. Similarly, Whaley et al., 2022 stated that the degree of stratospheric chemistry in the models did not reveal a consistent benefit or handicap when comparing the models with surface measurements. Here, the O_3 partial column comparisons show significant variation, although again, models largely underpredict FTIR measurements. The R^2, mean percent difference, and NRMSE are

Deleted: (a) Monthly mean FTIR (black) and modelled partial columns of O_3, from Eureka using model data that are the nearest in time to each FTIR measurement shown in Figure 13. Error bars represent the standard deviation of the monthly mean. (b) Mean percent difference by month. Error bars represent standard deviation of the monthly mean percent difference.…

Deleted: M

Deleted: 16

Deleted: of

Deleted: s

Deleted: 16

Deleted: (

Deleted: 3)

Deleted: Overall

Deleted: are largely underpredicted

relatively consistent, where models with a larger percent difference also have weaker correlations and higher NRMSEs. An exception to this is CESM, which has one of the smallest overall differences across the models and locations. However, in the model vs. FTIR plot(s) (and Figs. 12, C11-C14), CESM has considerable scatter above and below the line of best fit, resulting in a decreased mean difference, while also reducing R^2, unlike MRI-ESM2, which has a similar mean percent difference and NRMSE, but a stronger linear correlation.

To supplement the aircraft and satellite campaigns undertaken for the POLARCAT study, daily mean O_3 measurements from the FTIR instruments at Eureka and Thule were compared to MOZART-4 simulations in Wespes et al. (2012). When examining a partial column from the ground to 300 hPa (approximately 9 km), the smoothed model showed a bias of -15% relative to the FTIR. This is consistent with their analysis of aircraft observations, which revealed that the model underestimated O_3 by 5-15%. Results here are similar to those presented in Wespes et al. (2012), where across all the locations and models, 24 of the 55 model-measurement mean percent differences were within ±15% (see Table 4). The FTIR uncertainty for O_3 partial columns ranges from 3.9% to 8.2%; the overall mean percent difference for MATCH-SALSA falls within these uncertainty bounds for all locations, and CESM, DEHM, MATCH and MRI-ESM2 are within FTIR uncertainty for all locations but Ny Ålesund.

The AMAP SLCF Assessment Report finds that the multi-model mean of Arctic O_3 has a bias of +11 ± 3% relative to surface measurements (AMAP, 2021). When partitioning results by region, all the models had positive biases when compared to the surface measurements in Alaska and negative biases in Northern Europe, resulting in a relatively small mean bias across the Arctic as a whole (Whaley et al., 2022). Inaccuracies in long-range transport of O_3 and its precursors may have contributed to the increased discrepancy seen in the model-FTIR comparisons of the current study, particularly in partial columns with larger values. For example, the underestimation of CO may contribute to the negative bias in O_3 (see Figs. 9-10). Most models in AMAP (2021) show negative biases for Greenland and Northern European locations, which would correspond closer geographically with the FTIR sites examined here. When comparing the AMAP models to TES (Tropospheric Emission Spectrometer) and ACE-FTS satellite O_3 measurements, the biases are negative at lower altitudes, and become positive at higher altitudes (Whaley et al., 2022). AMAP model vs. ozonesonde comparisons showed similar elevated positive biases around 6-8 km of up to ±50%, again indicating that the models may produce too much O_3 from mid-latitude anthropogenic emissions or that there may be too much downward transport of O_3 from the stratosphere (Whaley et al., 2023). The best performance in that study came from the multi-model mean, which simulated O_3 within ± 8% throughout the troposphere.

Deleted: 15

Deleted: C9

Deleted: C12

Deleted: time-matched

Deleted: In the current study,

Deleted: The similarity of these results to those in Wespes et al. (2012) indicates that despite model updates in the last decade, model biases remain unchanged.

Deleted: 10

Deleted: 11

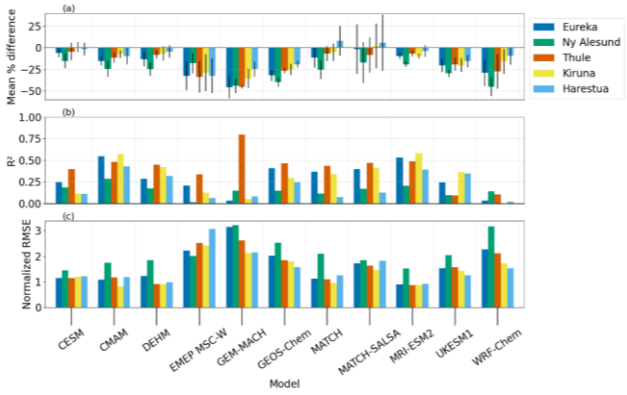

Figure 13: By model and location: (a) Overall model-measurement mean percent difference for O_3 0-7 km partial columns (Δ_O), with error bars that represent the standard deviation of the mean, as shown in the legend of Figs. C6-C10. (b) R^2 as shown in Fig 12 and Figs. C11-C14. (c) Normalized root-mean-square error.

Deleted: 14b, Fig.C5-C8

Deleted: 15

Deleted: C9-C12

Deleted: 17

Figure 14 shows the monthly MMM for O_3 at all locations, along with the monthly mean FTIR and the associated percent difference. This shows that the models, as a whole, have an increased negative bias in the middle of the year relative to the winter, while still exhibiting a negative bias overall. The longitudinal range of sites examined here may limit biases to be negative, not capturing the positive-negative gradient from west-east in O_3 found in the AMAP Report (AMAP, 2021; Whaley et al., 2022). Nonetheless, the model-FTIR O_3 comparisons reflect the proclivity of the models to underpredict Arctic O_3 in the lower troposphere, as also found in the aforementioned studies. The results of this study agree with results from previous studies and suggest that improvements are still needed for accurate modelling of O_3 and CO in the Arctic (Whaley et al., 2023). Models still require improvements in their treatment of stratospheric-tropospheric exchange and Arctic boundary layer processes to better simulate Arctic O_3, as well as further improvements and understanding about processes influencing O_3 removal through dry deposition and O_3 photochemical production from anthropogenic, biomass burning and natural sources in the lower and mid troposphere.

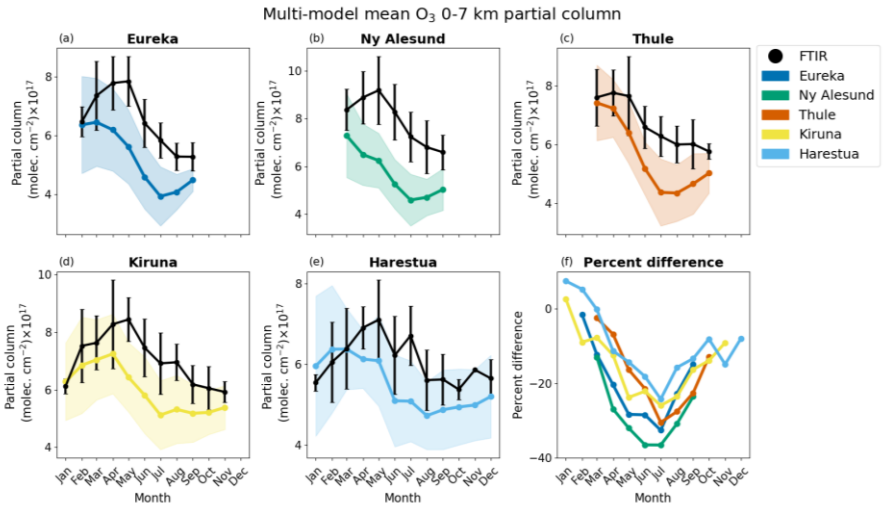

Figure 14: (a-e) Monthly mean FTIR (black) and multi-model mean (coloured) 0-7 km partial columns of O_3 ($PC_{F,monthly,j}$ and $PC_{MMM,monthly,j}$, respectively), with error bars and shaded areas representing the standard deviation of the mean. (f) Monthly mean percent difference of the MMM ($\Delta_{O,MMM}$) for all locations.

5 Conclusions

This study compares atmospheric models with data from five Arctic NDACC ground-based FTIR spectrometers. The models simulate SLCFs and precursor gases with 3-hourly outputs for the years 2008, 2009, 2014, and 2015. Here, a total of three models are evaluated for CH_4, nine for CO and 11 for O_3. The model simulations are compared with FTIR tropospheric partial column measurements to assess performance throughout the year and across locations.

Deleted: historical

Generally, across the five locations, the model simulations of 0-7 km partial columns of CH_4, CO and O_3 are underestimated. There were no significant patterns in the biases identified between the sites, species, or models examined. Modelled CH_4 partial columns are relatively consistent across the year, broadly capturing seasonal cycles, with the exception of a few outliers. CO simulations are inconsistent in reproducing the seasonal cycle, underpredicting springtime partial columns compared to the rest of the year, and skewing differences to be more positive when there are enhancements due to biomass burning events. Similarly, the models underestimated O_3 maxima more than O_3 minima in the troposphere. The multi-model means are reflective of these trends, for which (ignoring outliers), the CH_4 mean percent difference is relatively consistent across the year, CO has a maximum difference in the spring and a minimum in the summer, and O_3 has maximum difference centered around the summer. The AMAP SLCF Assessment Report found the best results using a multi-model mean for all

species when comparing with surface measurements (AMAP 2021; Whaley et al., 2022). However, here, the multi-model means of the tropospheric column for all species are biased low. The average MMM mean difference is approximately -10% for CH_4, -21% for CO and -18% for O_3 (see Table 5), where the uncertainty of the FTIR 0-7 km partial column is on the order of 6% on average. When examining the models and location pairs individually, the mean difference (inclusive of standard deviation) is within the respective FTIR uncertainty, for six of 15 model-FTIR comparisons for CH_4, 12 of 34 for CO, and 25 of 55 for O_3 (see Table 4).

Deleted: D1

Deleted: seven

These evaluations show that models are lacking some degree of transport and/or emissions to accurately reproduce tropospheric columns and seasonal variability in the Arctic. Model evaluation can provide a valuable checkpoint to help improve the representation of the Arctic in atmospheric models. NDACC FTIR spectrometers were selected for this project because of the wide range of species measured, high spectral resolution, multiple high-latitude sites, and publicly available data; in addition, the column-integrated FTIR measurements used in this study have a spatial and temporal footprint that is more representative of the free troposphere than in situ and satellite measurements. Future work would benefit from the inclusion of sensitivity studies, furthering the model-measurement comparisons with mid-latitude NDACC FTIR sites, and extending comparisons to a longer timeframe, with some models and locations having data from as early as 1990.

Table 4: Summary of model-measurement mean percent difference (Δ_O) for each model and location by species. MMM is the multi-model mean ($\Delta_{O,MMM}$). The colour scale indicates the mean percent difference relative to the FTIR measurements, from blue (-50%) to red (+50%). A square marker indicates that the mean percent difference is within the FTIR uncertainty. A triangle marker indicates that the mean difference is within the FTIR uncertainty combined with the standard deviation of the monthly mean percent difference.

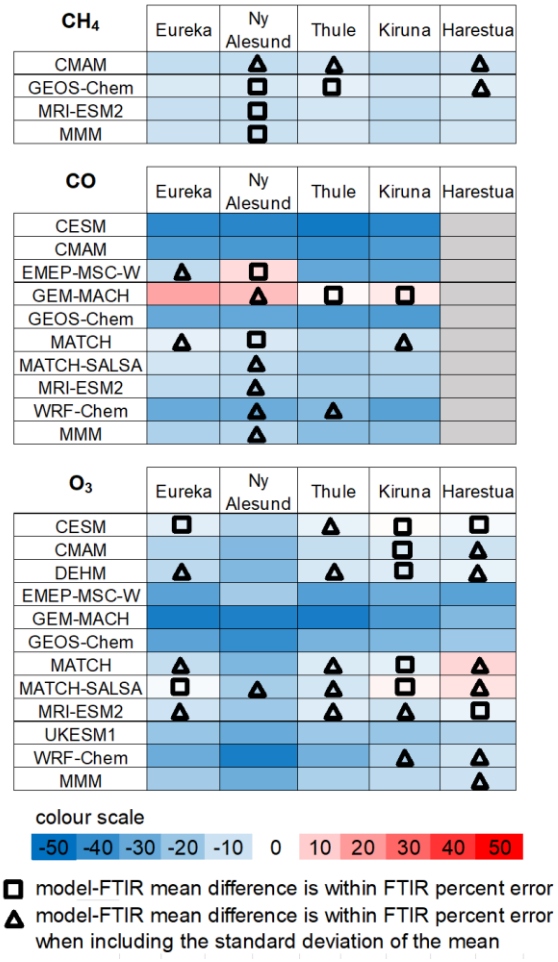

Table 5: The multi-model mean percent difference ($\Delta_{O,MMM}$) for each species at each location, including the overall average percent difference for each species and the standard deviation of the mean.

Gas	Location	MMM Percent Difference
CH_4	Eureka	-9.9 ± 0.7
	Ny Ålesund	-10.2 ± 0.7
	Thule	-7.5 ± 2.0
	Kiruna	-11.6 ± 0.5
	Harestua	-9.2 ± 1.4
	Average	-9.7
CO	Eureka	-17.6 ± 5.6
	Ny Ålesund	-16.7 ± 7.9
	Thule	-24.4 ± 6.5
	Kiruna	-23.7 ± 5.2
	Average	-20.6
O_3	Eureka	-20.1 ± 10.2
	Ny Ålesund	-28.5 ± 8.3
	Thule	-17.6 ± 9.8
	Kiruna	-14.6 ± 8.7
	Harestua	-9.6 ± 9.5
	Average	-18.1

880

Appendices

Appendix A – Additional figures for CH_4

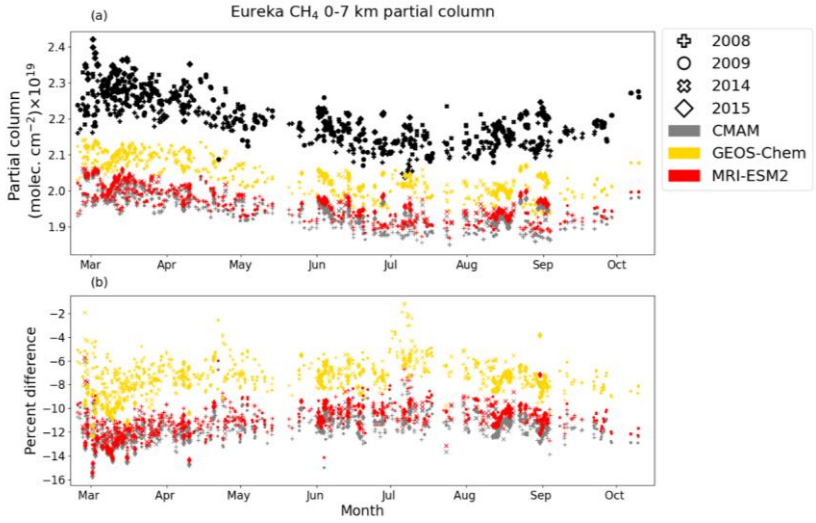

Figure A1: (a) FTIR (black) and smoothed model (colour) 0-7 km partial columns of CH_4 by day of year, from Eureka. Model data are the nearest in time to each FTIR measurement. (b) Model-measurement percent difference (Δ_i) from Eq. 2 by day of year. Each year is indicated by a different marker.

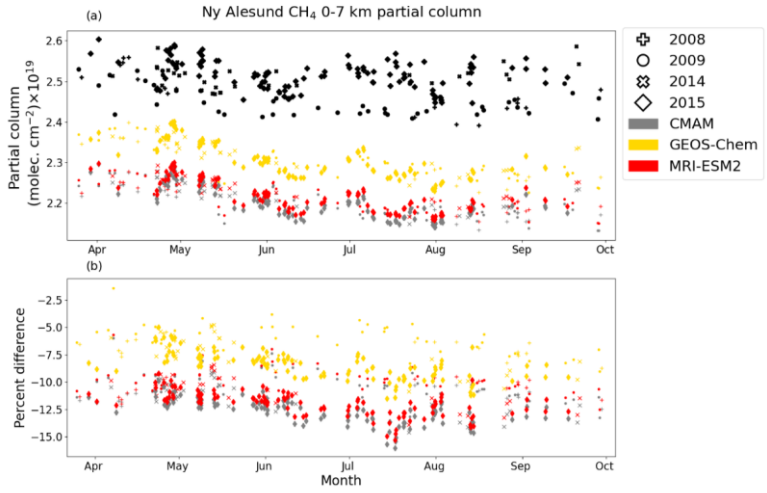

Figure A2: Same as Fig. A1 but for Ny Ålesund.

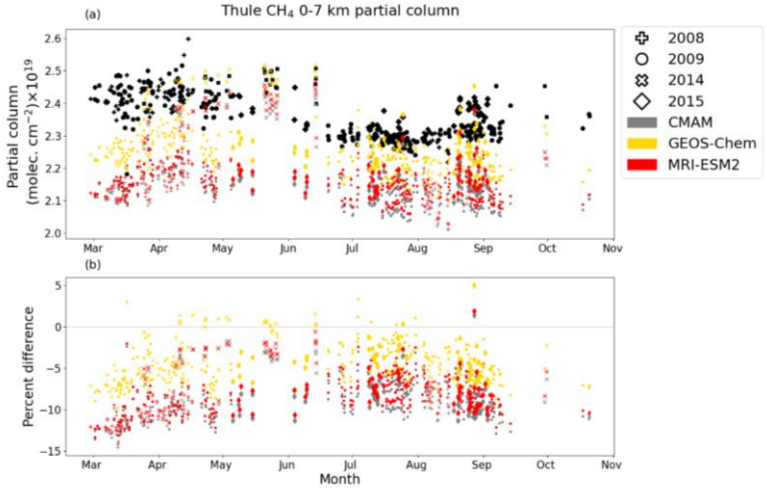

Figure A3: Same as Fig. A1 but for Thule.

Deleted: A1

Deleted: (a) FTIR (black) and modelled (colour) partial columns of CH_4 by day of year, from Ny Ålesund. Model data are the nearest in time to each FTIR measurement. (b) Percent difference from Eq. 2 by day of year. Each year is indicated by a different marker.

Deleted: A2

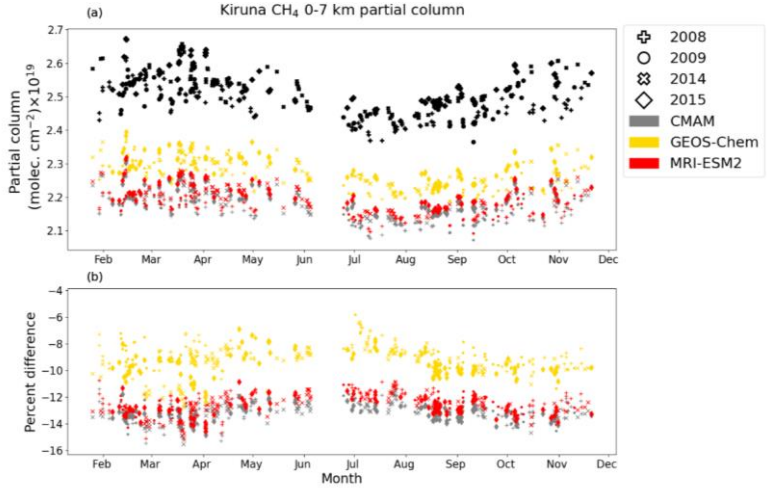

Figure A4: Same as Fig. A1 but for Kiruna.

Deleted: A3

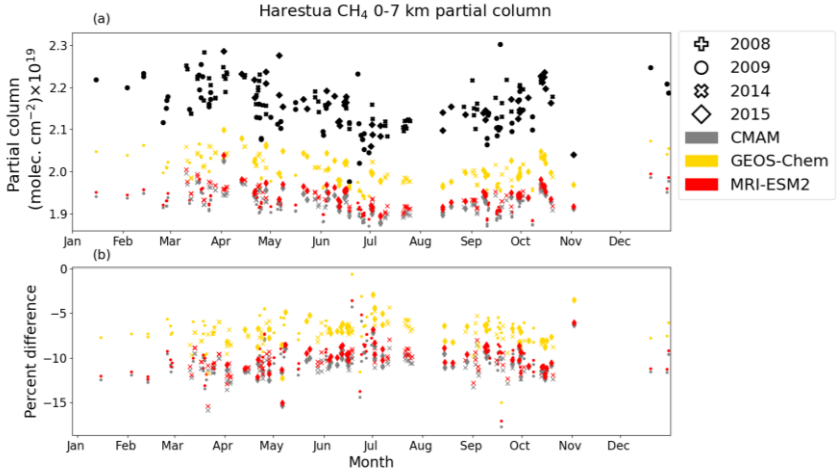

Figure A5: Same as Fig. A1 but for Harestua.

Deleted: A4

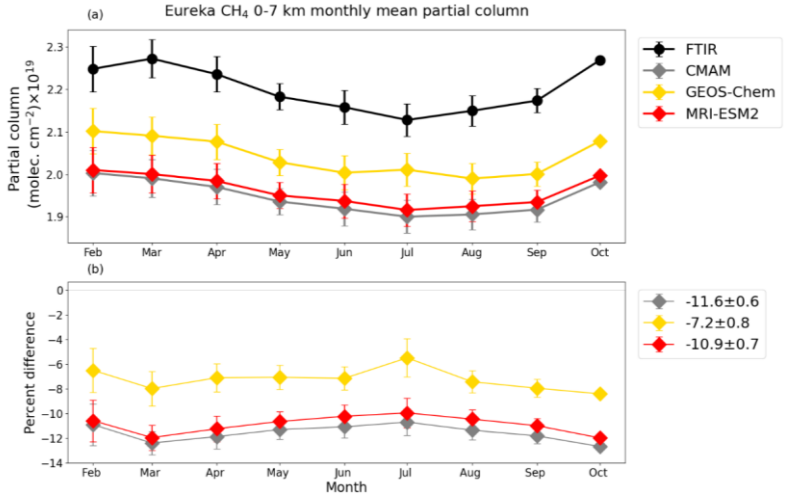

Figure A6: (a) Monthly mean FTIR (black) and smoothed model (colour) 0-7 km partial columns of CH_4 ($PC_{F,monthly,j}$ and $PC_{M,monthly,j}$, respectively), from Eureka using model data that are the nearest in time to each FTIR measurement shown in Figure A1. Error bars represent the standard deviation of the monthly mean. (b) Model-measurement mean percent difference by month ($\Delta_{monthly,j}$). Error bars represent standard deviation of the monthly mean percent difference. The legend on panel (b) shows the overall mean percent difference (Δ_O) with the standard deviation of the overall mean percent difference.

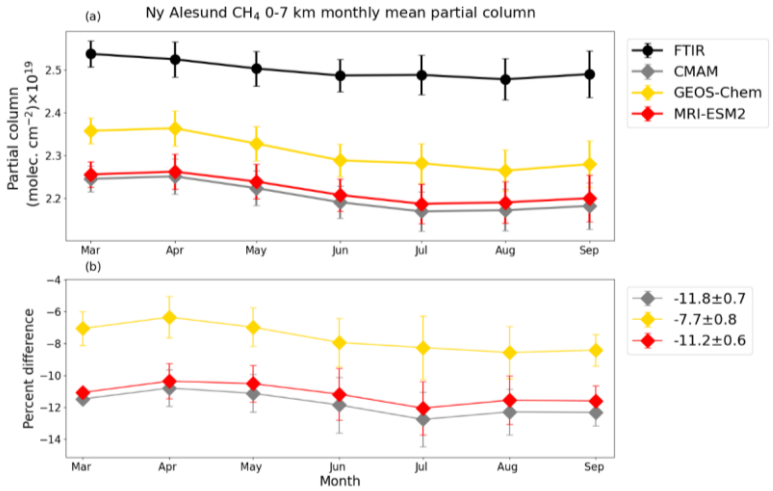

Figure A7: Same as Fig. A6 but for Ny Ålesund.

Deleted: Figure A5: (a) Monthly mean FTIR (black) and modelled (colour) partial columns of CH_4, from Ny Ålesund using model data that are the nearest in time to each FTIR measurement shown in Figure A1. Error bars represent the standard deviation of the monthly mean. (b) Mean percent difference by month. Error bars represent standard deviation of the monthly mean percent difference. The legend on panel (b) shows the overall mean percent difference with the standard deviation of the overall mean percent difference.¶

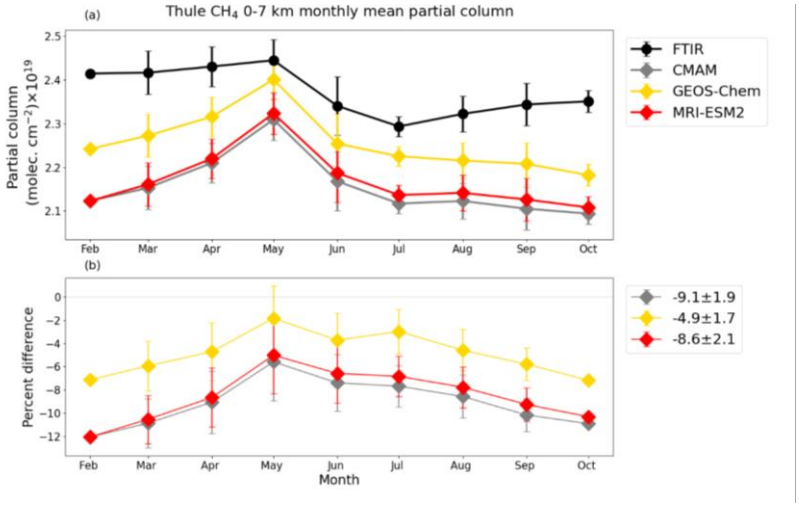

Figure A8: Same as Fig. A6 but for Thule.

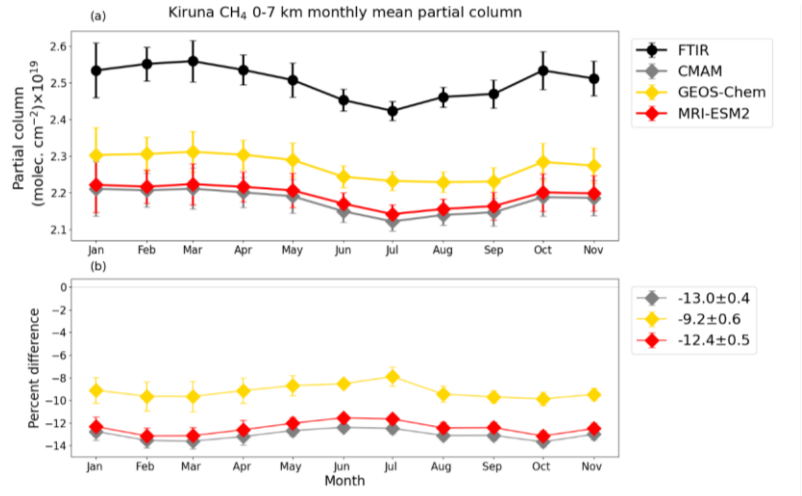

Figure A9: Same as Fig. A6 but for Kiruna.

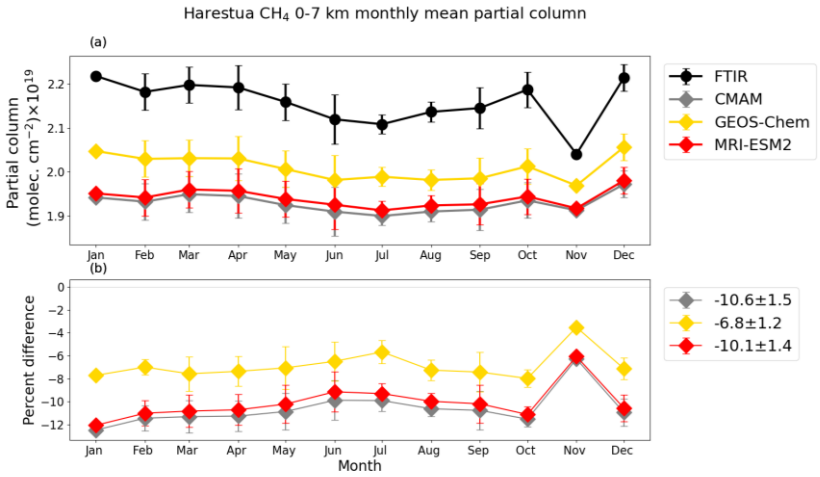

Figure A10: Same as Fig. A6 but for Harestua.

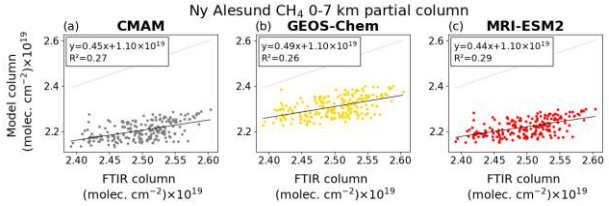

Figure A11: Smoothed model vs. FTIR 0-7 km partial column of CH_4 for Ny Ålesund, showing all available model-FTIR corresponding data. The black line is the line of best fit, where the equation and R^2 are noted in the legend. The 1:1 line is shown in light grey.

Deleted: A8
Deleted: A5
Deleted: A9
Deleted: M

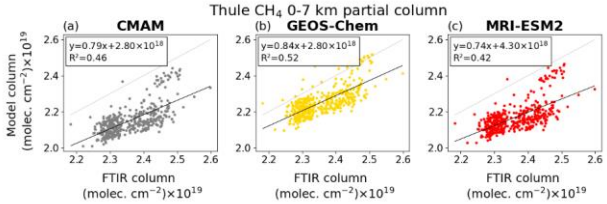

Figure A12: Same as Fig. A9 but for Thule.

Deleted: A10

955

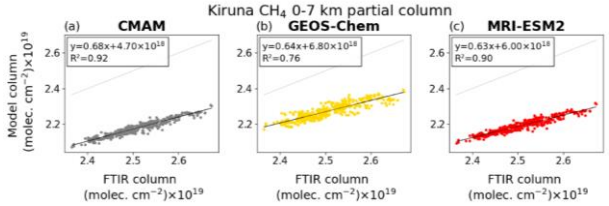

Figure A13: Same as Fig. A9 but for Kiruna.

Deleted: A11

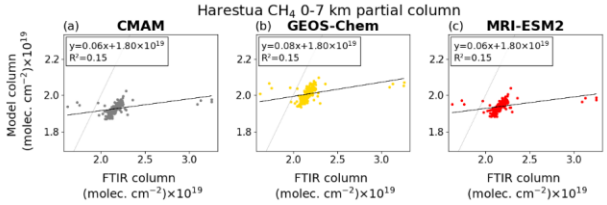

960

Figure A14: Same as Fig. A9 but for Harestua.

Deleted: A12

Appendix B – Additional figures for CO

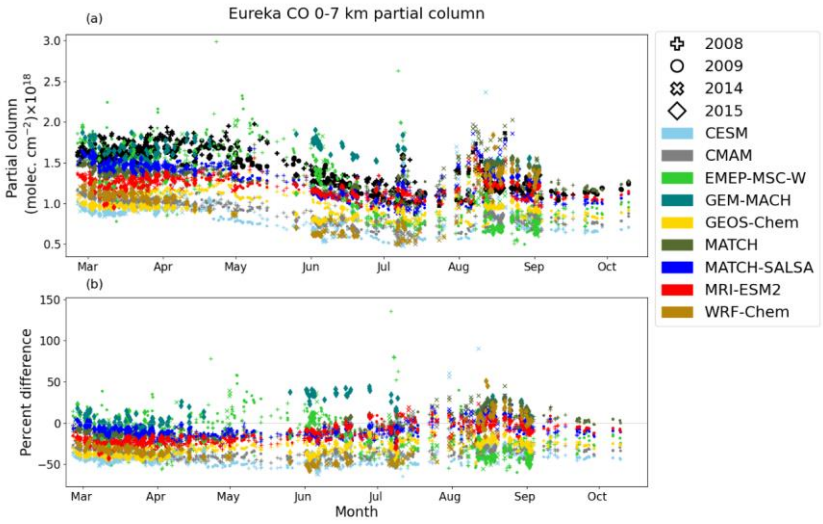

Figure B1: (a) FTIR (black) and smoothed model 0-7 km partial columns of CO by day of year, from Eureka. Model data are the nearest in time to each FTIR measurement. (b) Model-measureent percent difference (Δ_i) from Eq. 2 by day of year. Each year is indicated by a different marker.

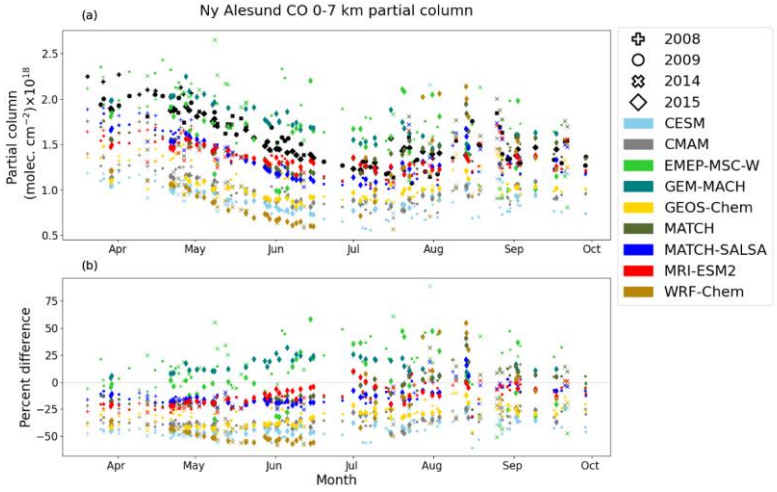

Figure B2: Same as Fig. B1 but for Ny Ålesund.

975

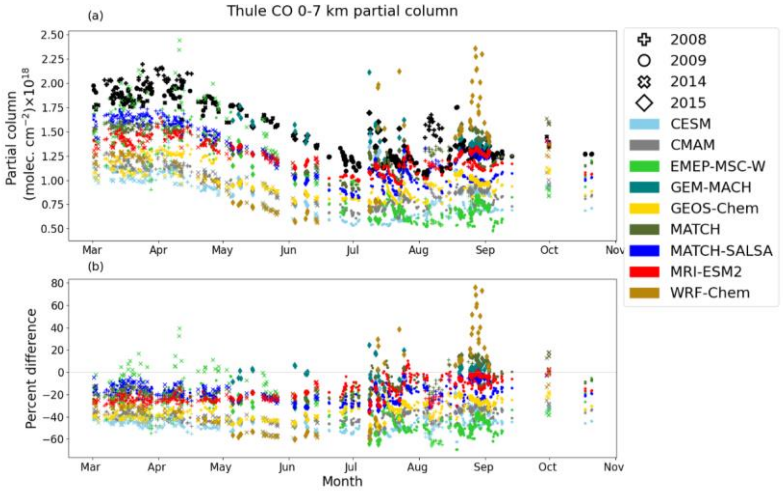

Figure B3: Same as Fig. B1 but for Thule.

Deleted: B2

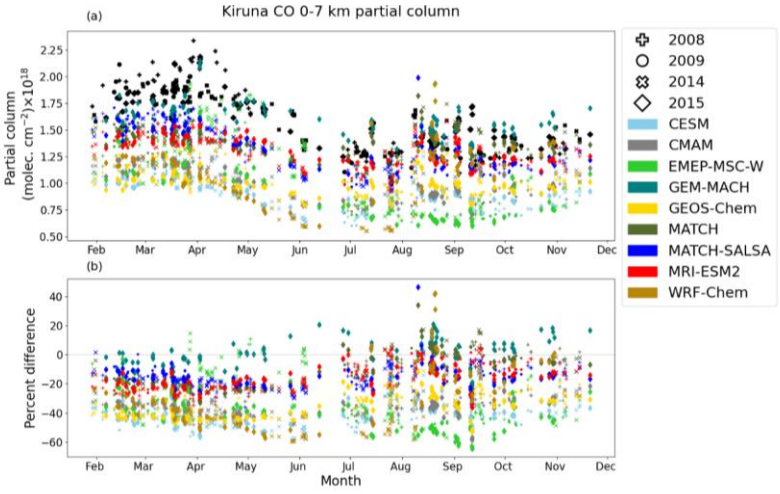

Figure B4: Same as Fig. B1 but for Kiruna.

Deleted: B3

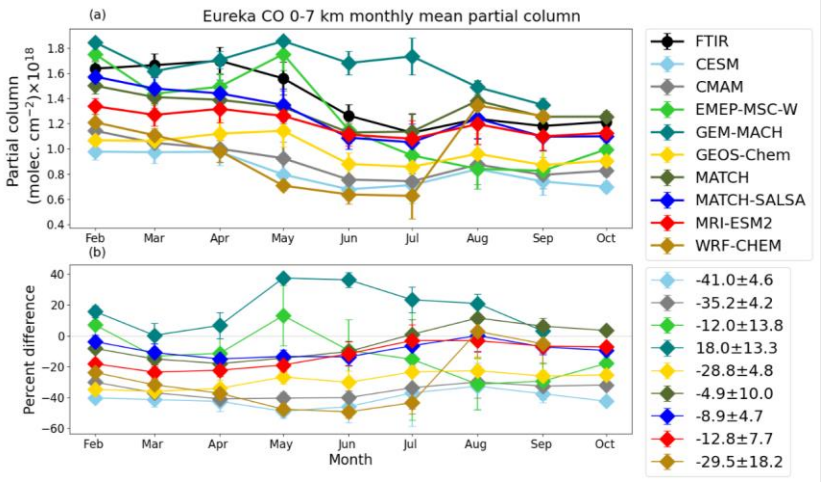

Figure B5: (a) Monthly mean FTIR (black) and smoothed model 0-7 km partial columns of CO ($PC_{F,monthly,j}$ and $PC_{M,monthly,j}$, respectively), from Eureka using model data that are the nearest in time to each FTIR measurement shown in Figure B1. Error bars represent the standard deviation of the monthly mean. (b) Model-measurement mean percent difference by month ($\Delta_{monthly,j}$). Error bars represent standard deviation of the monthly mean percent difference. The legend on panel (b) shows the overall mean percent difference (Δ_O) with the standard deviation of the overall mean percent difference.

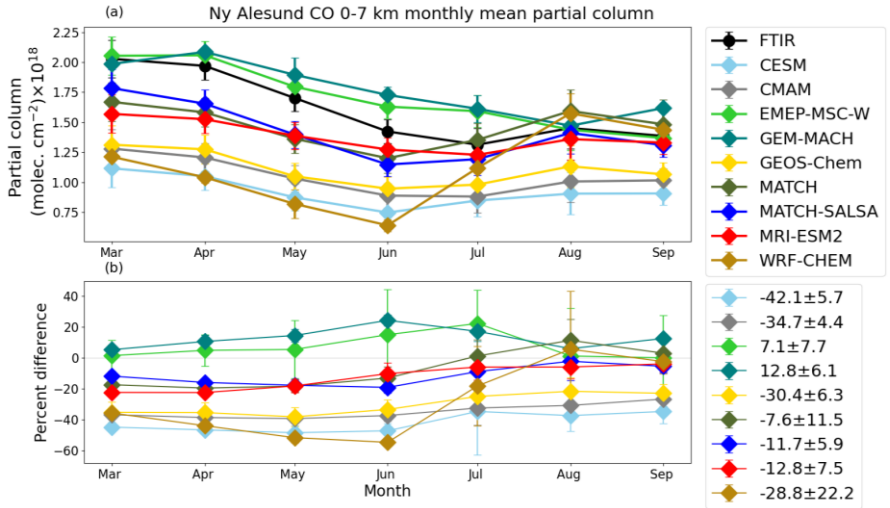

Figure B6: Same as Fig. B5 but for Ny Ålesund.

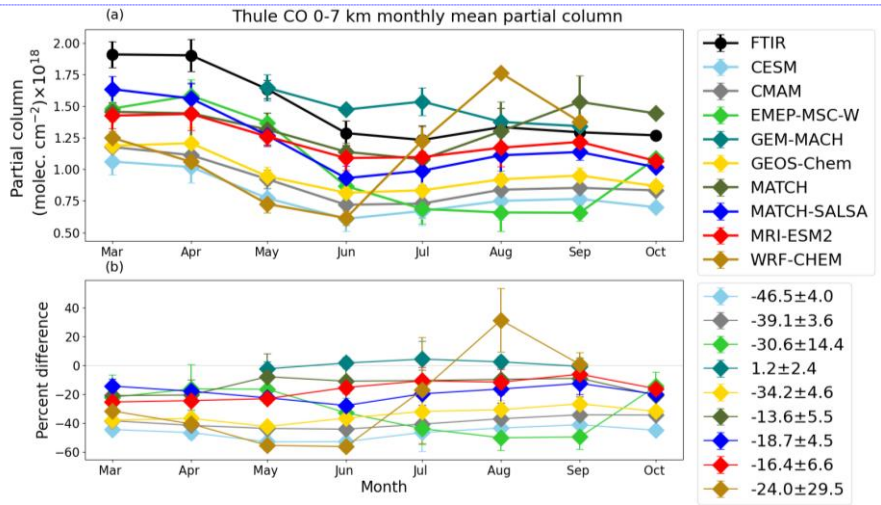

Figure B7: Same as Fig. B5 but for Thule.

Deleted: Figure B4: (a) Monthly mean FTIR (black) and modelled partial columns of CO, from Ny Ålesund using model data that are the nearest in time to each FTIR measurement shown in Figure B1. Error bars represent the standard deviation of the monthly mean. (b) Mean percent difference by month. Error bars represent standard deviation of the monthly mean percent difference. The legend on panel (b) shows the overall mean percent difference with the standard deviation of the overall mean percent difference.¶

Deleted: 5

Deleted: 4

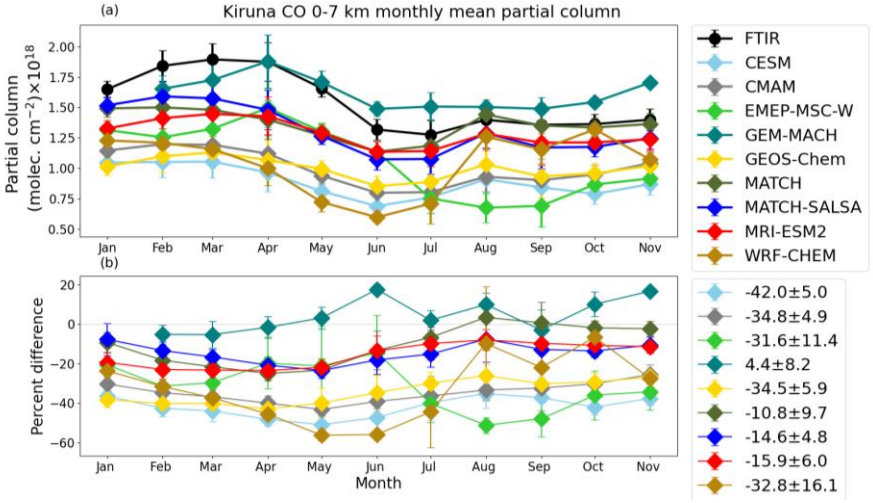

Figure B8: Same as Fig. B5 but for Kiruna.

Deleted: 6

Deleted: 4

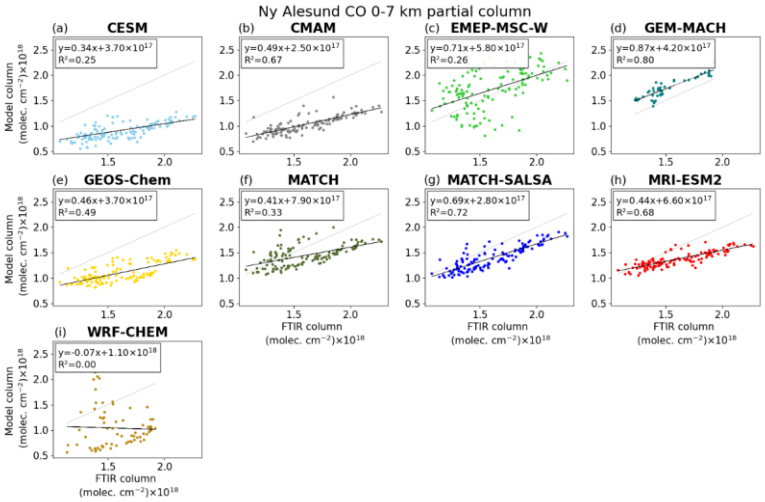

1015

Figure B9: Smoothed model vs. FTIR 0-7 km partial columns of CO for Ny Ålesund, showing all available model-FTIR corresponding data. The black line is the line of best fit, where the equation and R^2 are noted in the legend. The 1:1 line is shown in light grey.

Deleted: B7

Deleted: M

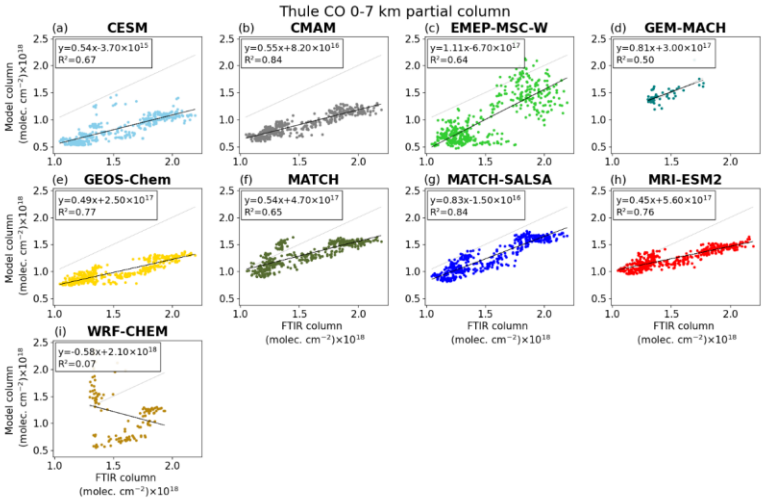

Figure B10: Same as Fig. B9 but for Thule.

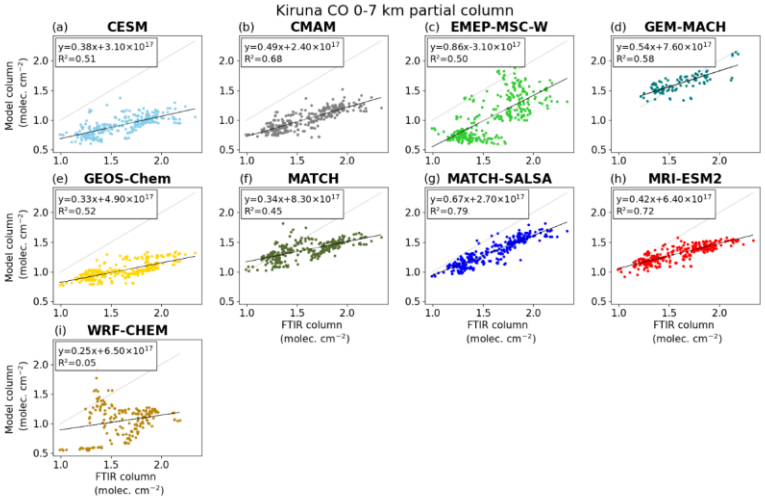

Figure B11: Same as Fig. B9 but for Kiruna.

Appendix C – Additional figures for O_3

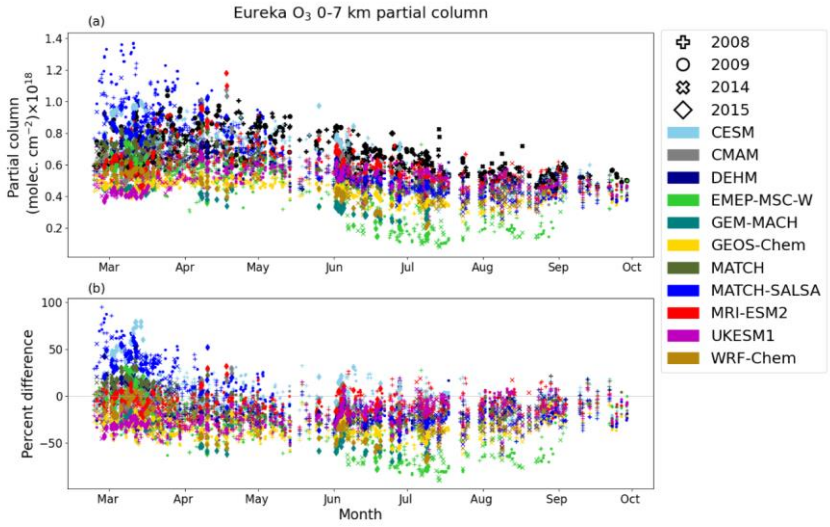

Figure C1: (a) FTIR (black) and smoothed model partial columns of O_3 by day of year, from Eureka. Model data are the nearest in time to each FTIR measurement. (b) Model-measureent percent difference (Δ_i) from Eq. 2 by day of year. Each year is indicated by a different marker.

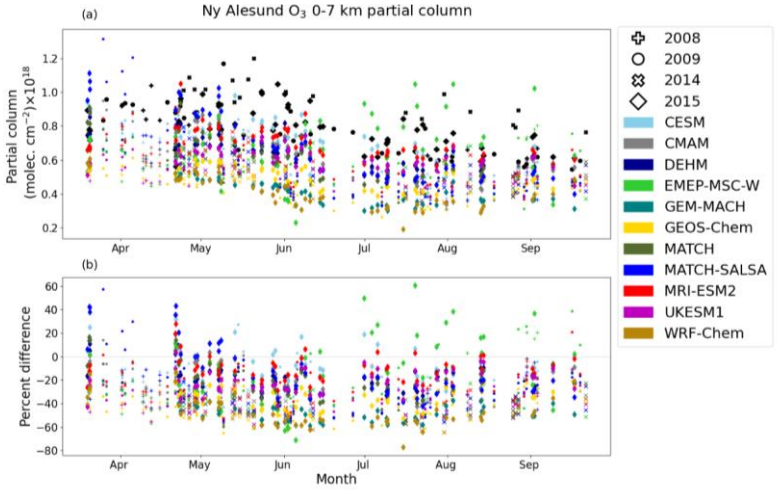

Figure C2: Same as Fig. C1 but for Ny Ålesund.

Deleted: **Figure C1: (a) FTIR (black) and modelled partial columns of O_3 by day of year, from Ny Ålesund. Model data are the nearest in time to each FTIR measurement. (b) Percent difference from Eq. 2 by day of year. Each year is indicated by a different marker.¶**

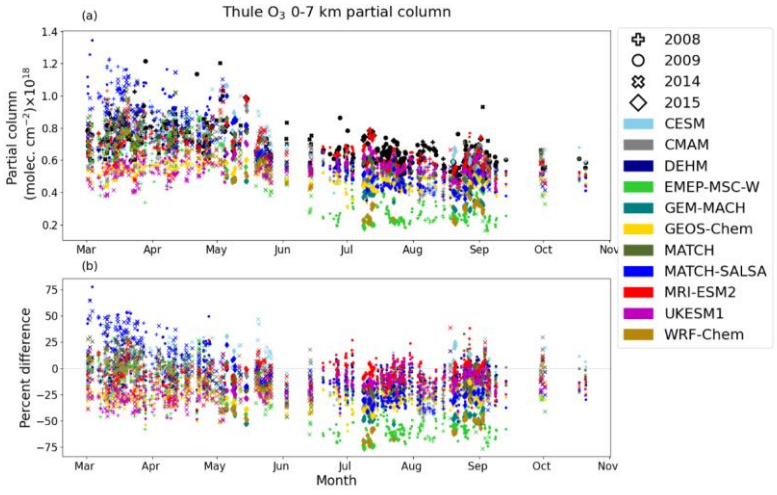

Figure C3: Same as Fig. C1 but for Thule.

Deleted: C2

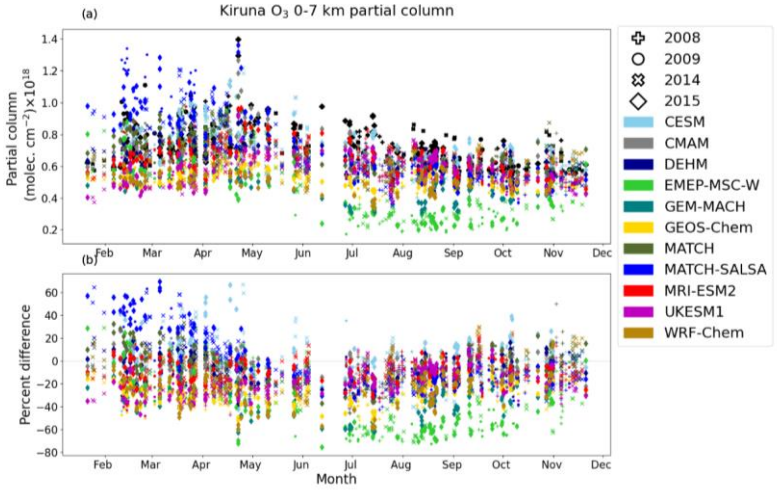

Figure C4: Same as Fig. C1 but for Kiruna.

Deleted: C3

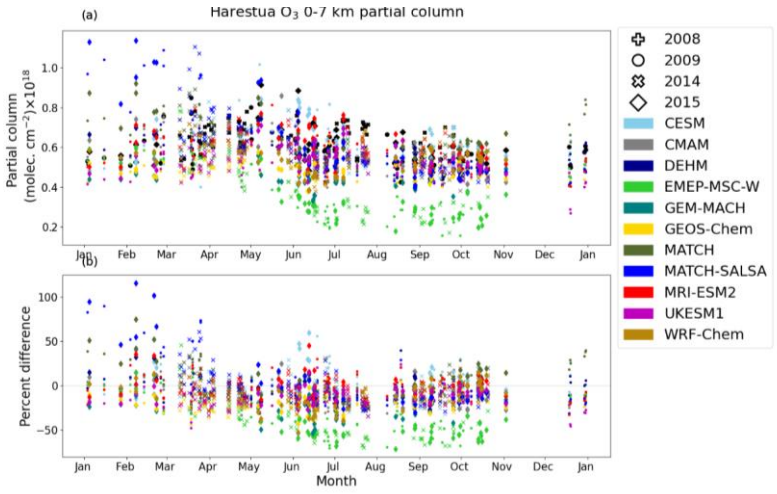

Figure C5: Same as Fig. C1 but for Harestua.

Deleted: C4

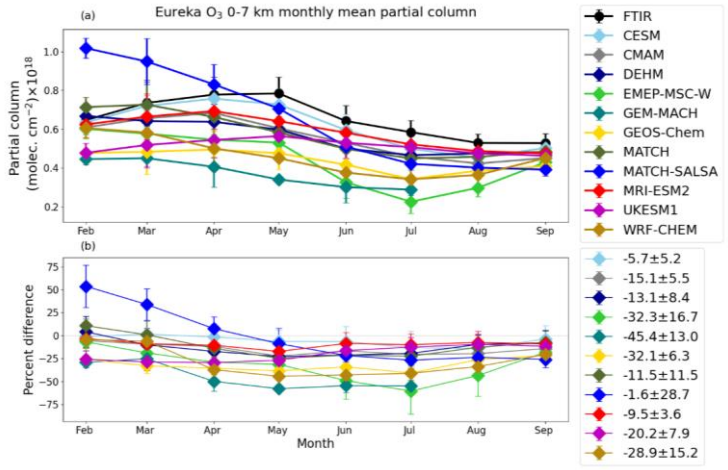

Figure C6: (a) Monthly mean FTIR (black) and smoothed model 0-7 km partial columns of O_3 ($PC_{F,monthly,j}$ and $PC_{M,monthly,j}$, respectively) from Eureka using model data that are the nearest in time to each FTIR measurement shown in Figure C1. Error bars represent the standard deviation of the monthly mean. (b) Model-measurement mean percent difference by month ($\Delta_{monthly,j}$). Error bars represent standard deviation of the monthly mean percent difference. The legend on panel (b) shows the overall mean percent difference (Δ_O) with the standard deviation of the overall mean percent difference.

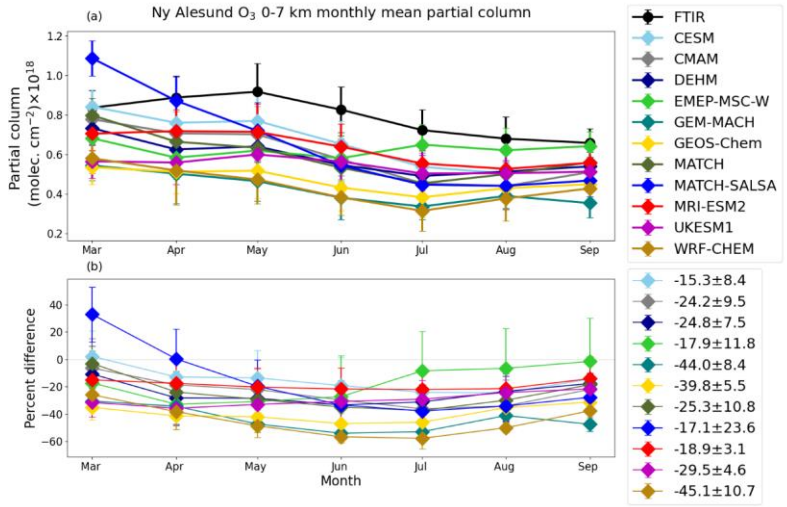

1065

Figure C7: Same as Fig. C6 but for Thule.

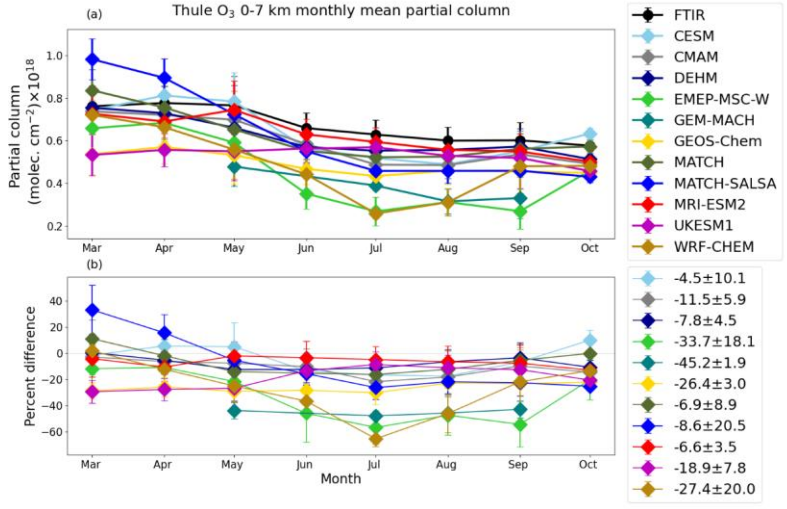

Figure C8: Same as Fig. C6 but for Thule.

Deleted: C6

Deleted: C5

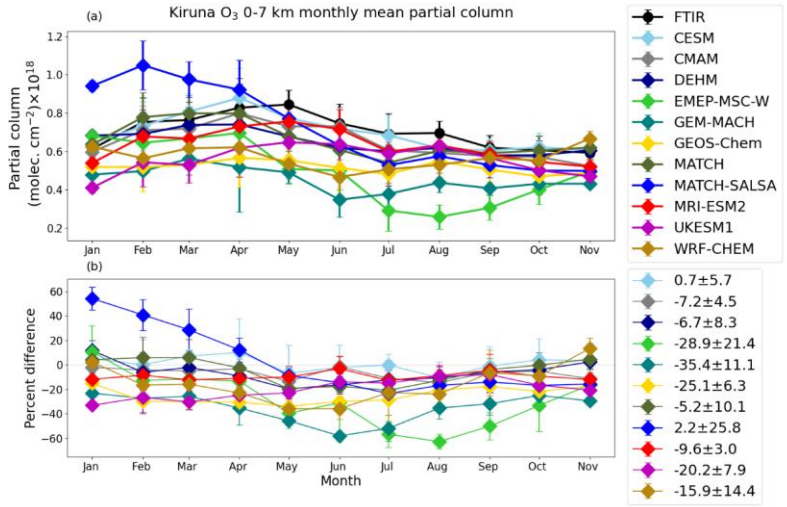

Figure C9: Same as Fig. C6 but for Kiruna.

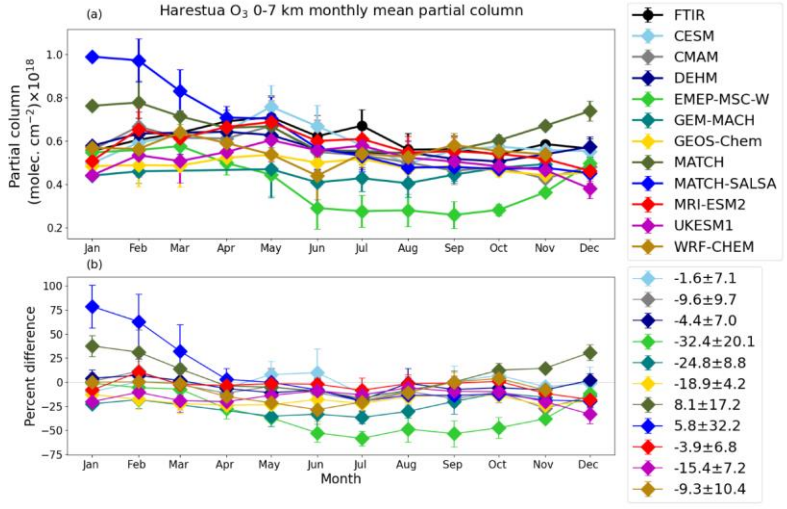

Figure C10: Same as Fig. C6 but for Harestua.

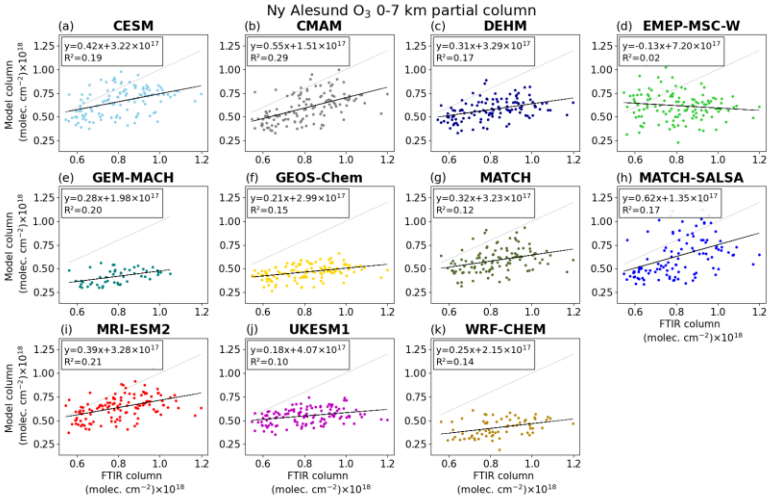

Figure C11: Model vs. FTIR 0-7 km partial columns of O_3 for Ny Ålesund, showing all available model-FTIR corresponding data. The black line is the line of best fit, where the equation and R^2 are noted in the legend. T The 1:1 line is shown in light grey.

Deleted: C9

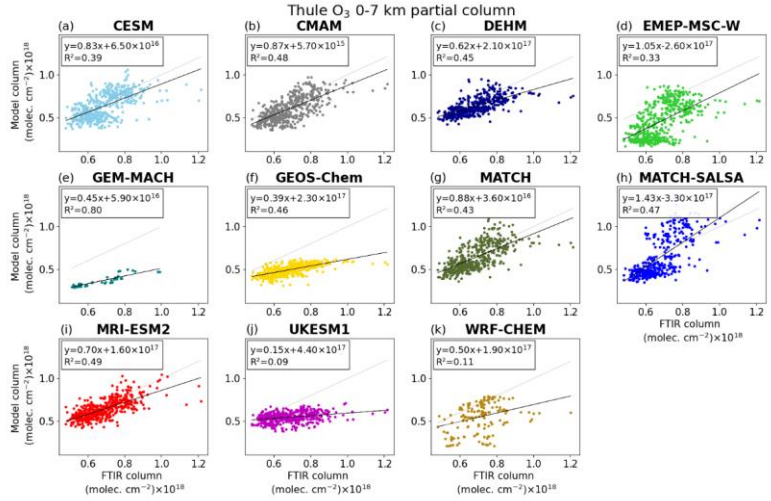

Figure C12: Same as Fig. C11 but for Thule.

Deleted: C10

Deleted: C9

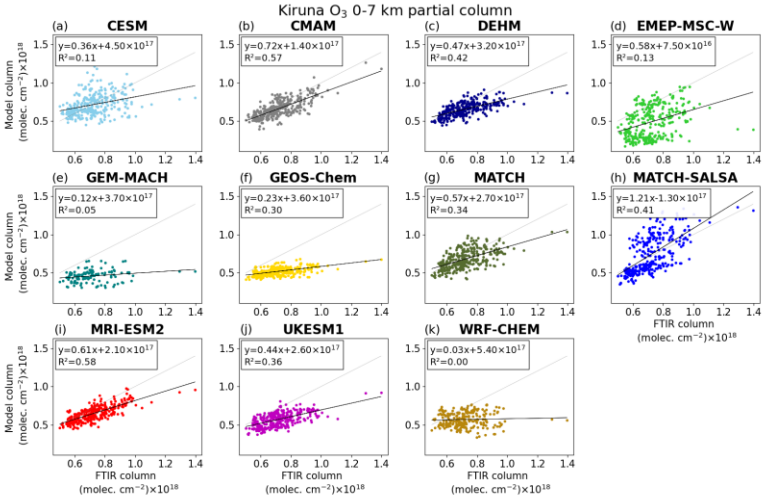

Figure C13: Same as Fig. C11 but for Kiruna.

Deleted: C11

Deleted: C9

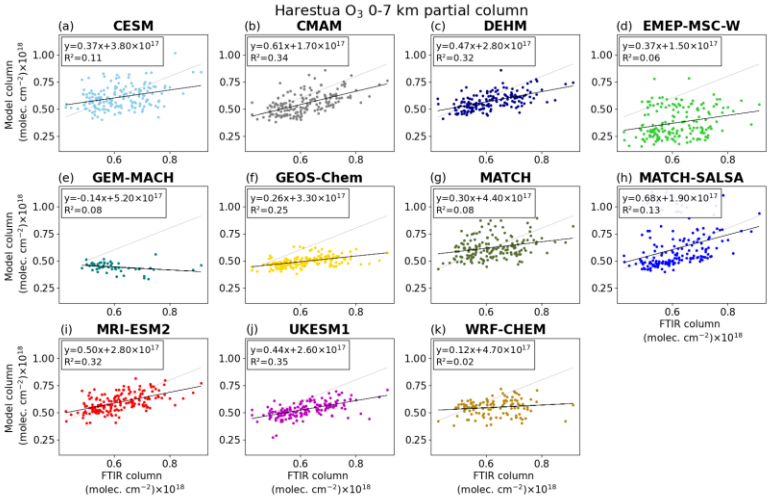

Figure C14: Same as Fig. C11 but for Harestua.

Deleted: C12

Deleted: C9

Deleted: Appendix D – MMM summary table¶

Deleted: Table D1: The multi-model mean percent difference for each species at each location, including the overall average percent difference for each species and the standard deviation of the mean.¶
Gas ...

Data availability

The FTIR data are publicly available on the NDACC data repository (https://www-air.larc.nasa.gov/missions/ndacc/data.html (last access: 14 Feb 2023), and the model data are available at https://doi.org/10.18164/e0a0ac5c-d851-45b9-b6d9-4abc29d7d419 (last access: 14 Feb 2023).

Author contribution

KAW, CHW, and KS conceived this project. VF performed the formal analysis, including the comparisons between datasets, formation of plots and tables, and writing the manuscript. KS, CHW, and KAW provided scientific guidance and support throughout the work in addition to comments and edits to the manuscript. TB, JWH, JM, JN, MP and ANR provided advice on the FTIR data and facilitated the operations and data management for their respective instruments. SA, SB, RYC, JC, MD, SD, XD, JSF, MG, WG, JL, KSL, LM, TO, NO, DAP. LP, JCR, MAT, ST and ST provided the model outputs for the AMAP report and guidance on the analysis of models. All co-authors provided feedback on the paper.

Competing interests

At least one of the co-authors is a member of the editorial board of Atmospheric Measurement Techniques. The peer-review process was guided by an independent editor, and the authors also have no other competing interests to declare.

Disclaimer

Publisher's note: Copernicus Publications remains neutral with regard to jurisdictional claims in published maps and institutional affiliations.

Acknowledgements

Funding for this work was provided by the Canadian Space Agency under the Earth System Science Data Analyses Program (grant 21SUASABBC).

The authors acknowledge the use of model datasets from the 2021 AMAP SLCF Assessment Report. The authors would like to thank all the people involved with the data collection and maintenance of the high-latitude NDACC FTIR instruments used in this study.

The Eureka FTIR measurements were made at the Polar Environment Atmospheric Research Laboratory (PEARL) by the Canadian Network for the Detection of Atmospheric Composition Change (CANDAC), which has been supported by the Atlantic Innovation Fund/Nova Scotia Research Innovation Trust, Canada Foundation for Innovation, Canadian Foundation for Climate and Atmospheric Sciences, Canadian Space Agency, Environment and Climate Change Canada (ECCC), Government of Canada International Polar Year funding, Natural Sciences and Engineering Research Council, Northern Scientific Training Program, Ontario Innovation Trust, Polar Continental Shelf Program, and Ontario Research Fund. We thank former CANDAC/PEARL PI James Drummond, PEARL Site Manager Pierre Fogal, CANDAC Data Manager Yan Tsehtik, the CANDAC operators, and the staff at ECCC's Eureka Weather Station for their contributions to data acquisition, and for logistical and on-site support.

We gratefully acknowledge funding from the Transregional Collaborative Research Centre TR 172 -- Arctic Amplification: Climate Relevant Atmospheric and Surface Processes $(AC)^3$, project E02: Ny-Ålesund Column Thermodynamic Structure, Clouds, Aerosols, Trace Gases and Radiative Effects. We also thank the Senate of Bremen for financial support. The AWI Bremerhaven provided logistical support for measurements in Ny Ålesund.

KIT would like to thank Uwe Raffalski from the Swedish Institute of Space Physics (IRF) for their continuing support of the NDACC FTIR site Kiruna.

MG and ST received financial support from the Arctic Monitoring and Assessment Programme (AMAP).

KSL, JCR, LM, and TO (LATMOS) acknowledge support from EU iCUPE (Integrating and Comprehensive Understanding on Polar Environments) project (grant agreement no. 689443) under the European Network for Observing our Changing Planet (ERA-Planet) and from access to IDRIS HPC resources (GENCI allocation A009017141) as well as the IPSL mesoscale computing center (CICLAD: Calcul Intensif pour le CLimat, l'Atmosphère et la Dynamique) for model simulations. KSL also acknowledges support from French Space Agency (CNES) MERLIN (contract 7752).

MD and NO were supported by the Environment Research and Technology Development Fund (JPMEERF20202003 and JPMEERF20232001) of the Environmental Restoration and Conservation Agency Provided by the Ministry of Environment of Japan, the Arctic Challenge for Sustainability II (ArCS II), Program Grant Number JPMXD1420318865, and a grant for the Global Environmental Research Coordination System from the Ministry of the Environment, Japan (MLIT2253).

Deleted: JPMEERF20205001

References

Amann, M., Bertok, I., Borken-Kleefled, J., Cofala, J., Heyes, C., Höglund-Isaksson, L., Klimont, Z., Nguyen, B., Posch, M., Rafaj, P., Sandler, R., Schöpp, W., Wagner, F., and Winiwarter, W.: Cost-effective control of air quality and greenhouse gases in Europe: Modelling and policy applications, Environ. Modell. Softw., 26, 1489–1501, https://doi.org/10.1016/j.envsoft.2011.07.012, 2011.

AMAP, 2021. AMAP Assessment 2021: Impacts of Short-lived Climate Forcers on Arctic Climate, Air Quality, and Human Health. Arctic Monitoring and Assessment Programme (AMAP), Tromsø, Norway, viii + 324pp, https://www.amap.no/documents/doc/amap-assessment-2021-impacts-of-short-lived-climate-forcers-on-arctic-climate-air-quality-and-human-health/3614, 2021.

Andersson, C., Langner, J., and Bergström, R.: Interannual variation and trends in air pollution over Europe due to climate variability during 1958-2001 simulated with a regional CTM coupled to the ERA-40 reanalysis, Tellus B, 59, 77–98, https://doi.org/10.1111/j.1600-0889.2006.00231, 2007.

Batchelor, R. L., Strong, K., Lindenmaier, R., Mittermeier, R. L., Fast, H., Drummond, J. R., and Fogal, P. F.: A new Bruker IFS 125HR FTIR spectrometer for the Polar Environment Atmospheric Research Laboratory at Eureka, Nunavut, Canada: measurements and comparison with the existing Bomem DA8 spectrometer, J. Atmos. Ocean. Tech., 26, 1328–1340, https://doi.org/10.1175/2009JTECHA1215.1, 2009.

Berg, T., Sekkesaeter, S., Steinnes, E., Valdal, A. K., Wibetoe, G.: Springtime depletion of mercury in the European Arctic as observed at Svalbard, Sci. Total Environ., 304, 43–51, https://doi.org/10.1016/S0048-9697(02)00555-7, 2003.

Bey, I., Jacob, D. J., Yantosca, R. M., Logan, J. A., Field, B. D., Fiore, A. M., Li, Q., Liu, H. Y., Mickley, L. J., and Schultz, M. G.: Global modeling of tropospheric chemistry with assimilated meteorology: Model description and evaluation, J. Geophys. Res., 106, 23073–23095, https://doi.org/10.1029/2001JD000807, 2001.

Blumenstock, T. H., Fisher, H., Friedle, A., Hase, F., and Thomas, P.: Column Amounts of $ClONO_2$, HCl, HNO_3, and HF from Ground-Based FTIR Measurements Made Near Kiruna, Sweden, in Late Winter 1994, J. Atmos. Chem., 26, 311–321, https://doi.org/10.1023/A:1005728713762, 1997.

Blumenstock, T., Hase, F., Kramer, I., Mikuteit, S., Fischer, H., Goutail, F., and Raffalski, U.: Winter to winter variability of chlorine activation and ozone loss as observed by ground-based FTIR measurements at Kiruna since winter 1993/94, Int. J. Remote Sens., 30, 4055–4064, https://doi.org/10.1080/01431160902821916, 2009.

Brandt, J., Silver, J., Frohn, L. M., Geels, C., Gross, A., Hansen, A. B., Hansen, K. M., Hedegaard, G. B., Skjøoth, C. A., Villadsen, H., Zare, A., and Christensen, J. H.: An integrated model study for Europe and North America using the Danish Eulerian Hemispheric Model with focus on intercontinental al transport of air pollution, Atmos. Environ., 53, 156–176, https://doi.org/10.1016/j.atmosenv.2012.01.011 2012.

Bush, E. and Lemmen, D.S., editors (2019): Canada's Changing Climate Report; Government of Canada, Ottawa, ON. 444 p. https://changingclimate.ca/CCCR2019/, (last access: 2 Feb 2023), 2019.

Christensen, J. H.: The Danish Eulerian hemispheric model – A three-dimensional air pollution model used for the Arctic, Atmos. Environ., 31, 4169–4191, https://doi.org/10.1016/S1352-2310(97)00264-1 , 1997.

Danabasoglu, G., Lamarque, J., Bacmeister, J., Bailey, D. A., DuVivier, A. K., and Edwards, J.: The Community Earth System Model Version 2 (CESM2), J. Adv. Model. Earth Sy., 12, e2019MS001916, https://doi.org/10.1029/2019MS001916, 2020.

De Mazière, M., Thompson, A. M., Kurylo, M. J., Wild, J. D., Bernhard, G., Blumenstock, T., Braathen, G. O., Hannigan, J. W., Lambert, J.-C., Leblanc, T., McGee, T. J., Nedoluha, G., Petropavlovskikh, I., Seckmeyer, G., Simon, P. C., Steinbrecht, W., and Strahan, S. E.: The Network for the Detection of Atmospheric Composition Change (NDACC): history, status and perspectives, Atmos. Chem. Phys., 18, 4935–4964, https://doi.org/10.5194/acp-18-4935-2018, 2018.

Emmons, L. K., Arnold, S. R., Monks, S. A., Huijnen, V., Tilmes, S., Law, K. S., Thomas, J. L., Raut, J.-C., Bouarar, I., Turquety, S., Long, Y., Duncan, B., Steenrod, S., Strode, S., Flemming, J., Mao, J., Langner, J., Thompson, A. M., Tarasick, D., Apel, E. C., Blake, D. R., Cohen, R. C., Dibb, J., Diskin, G. S., Fried, A., Hall, S. R., Huey, L. G., Weinheimer, A. J., Wisthaler, A., Mikoviny, T., Nowak, J., Peischl, J., Roberts, J. M., Ryerson, T., Warneke, C., and Helmig, D.: The POLARCAT Model Intercomparison Project (POLMIP): overview and evaluation with observations, Atmos. Chem. Phys., 15, 6721–6744, https://doi.org/10.5194/acp-15-6721-2015, 2015.

Emmons, L. K., Walters, S., Hess, P. G., Lamarque, J.-F., Pfister, G. G., Fillmore, D., Granier, C., Guenther, A., Kinnison, D., Laepple, T., Orlando, J., Tie, X., Tyndall, G., Wiedinmyer, C., Baughcum, S. L., and Kloster, S.: Description and evaluation of the Model for Ozone and Related chemical Tracers, version 4 (MOZART-4), Geosci. Model Dev., 3, 43–67, https://doi.org/10.5194/gmd-3-43-2010, 2010.

Eneroth, K., Holmén, K., Berg, T., Schmidbauer, N., and Solberg, S.: Springtime depletion of tropospheric ozone, gaseous elemental mercury and non-methane hydrocarbons in the European Arctic, and its relation to atmospheric transport, Atmos. Environ., 41, 8511–8526, https://doi.org/10.1016/j.atmosenv.2007.07.008, 2007.

Fisher, J. A., Jacob, D. J., Purdy, M. T., Kopacz, M., Le Sager, P., Carouge, C., Holmes, C. D., Yantosca, R. M., Batchelor, R. L., Strong, K., Diskin, G. S., Fuelberg, H. E., Holloway, J. S., Hyer, E. J., McMillan, W. W., Warner, J., Streets, D. G., Zhang, Q., Wang, Y., and Wu, S.: Source attribution and interannual variability of Arctic pollution in spring constrained by aircraft (ARCTAS, ARCPAC) and satellite (AIRS) observations of carbon monoxide, Atmos. Chem. Phys., 10, 977–996, https://doi.org/10.5194/acp-10-977-2010, 2010.

Galle, B., Mellqvist, J., Arlander, D. W., Fløisand, I., Chipperfield, M. P., and Lee, A. M.: Ground Based FTIR Measurements of stratospheric species from Harestua, Norway during SESAME and Comparison with Models, J. Atmos. Chem., 32, 147–164, https://doi.org/10.1023/A:1006137924562, 1999.

Gong, W., Makar, P. A., Zhang, J., Milbrandt, J., Gravel, S., Hayden, K. L., Macdonald, A. M., and Leaitch, W. R.: Modelling aerosol cloud meteorology interaction: A case study with a fully coupled air quality model GEM-MACH, Atmos. Environ., 115, 6 95–715, https://doi.org/10.1016/j.atmosenv.2015.05.062, 2015.

Gong, W., Beagley, S. R., Cousineau, S., Sassi, M., Munoz-Alpizar, R., Ménard, S., Racine, J., Zhang, J., Chen, J., Morrison, H., Sharma, S., Huang, L., Bellavance, P., Ly, J., Izdebski, P., Lyons, L., and Holt, R.: Assessing the impact of shipping emissions on air pollution in the Canadian Arctic and northern regions: current and future modelled scenarios, Atmos. Chem. Phys., 18, 16653– 16687, https://doi.org/10.5194/acp-18-16653-2018, 2018.

Hannigan, J. W., Coffey, M. T., and Goldman, A.: Semiautonomous FTS Observation System for Remote Sensing of Stratospheric and Tropospheric Gases, J. Atmos. Ocean. Tech., 26, 1814–1828, https://doi.org/10.1175/2009JTECHA1230.1, 2009.

Hase, F., Hannigan, J. W., Coffey, M. T., Goldman, A., Höpfner, M., Jones, N. B., Rinsland, C. P., and Wood, S. W.: Intercomparison of retrieval codes used for the analysis of high-resolution, ground-based FTIR measurements, J. Quant. Spectrosc. Ra., 87, 25–52, https://doi.org/10.1016/j.jqsrt.2003.12.008, 2004.

Hirdman, D., Sodemann, H., Eckhardt, S., Burkhart, J. F., Jefferson, A., Mefford, T., Quinn, P. K., Sharma, S., Ström, J., and Stohl, A.: Source identification of short-lived air pollutants in the Arctic using statistical analysis of measurement data and particle dispersion model output, Atmos. Chem. Phys., 10, 669–693, https://doi.org/10.5194/acp-10-669-2010, 2010.

Höglund-Isaksson, L., Gómez-Sanabria, A., Klimont, Z., Rafaj, P., and Schöpp, W.: Technical potentials and costs for reducing global anthropogenic methane emissions in the 2050 timeframe – results from the GAINS model, Environmental Research Communications, 2, 025004, https://doi.org/10.1088/2515- 7620/ab7457, 2020.

IPCC, 2021: Climate Change 2021: The Physical Science Basis. Contribution of Working Group I to the Sixth Assessment Report of the Intergovernmental Panel on Climate Change [Masson-Delmotte, V., P. Zhai, A. Pirani, S.L. Connors, C. Péan, S. Berger, N. Caud, Y. Chen, L. Goldfarb, M.I. Gomis, M. Huang, K. Leitzell, E. Lonnoy, J.B.R. Matthews, T.K. Maycock, T. Waterfield, O. Yelekçi, R. Yu, and B. Zhou (eds.)]. Cambridge University Press, Cambridge, United Kingdom and New York, NY, USA, 2391 pp. doi:10.1017/9781009157896, 2021.

IRWG, 2020. Infrared Working Group Retrieval Code, SFIT - SFIT Spectral Data Analysis Model. URL https://wiki.ucar.edu/display/sfit4/ (last access: 2 Feb 2023).

Jonsson, A. I., de Grandpré, J., Fomichev, V. I., McConnell, J. C., and Beagley, S. R.: Doubled CO2-induced cooling in the middle atmosphere: Photochemical analysis of the ozone radiative feedback, J. Geophys. Res., 109, D24103, https://doi.org/10.1029/2004JD005093, 2004.

Kalnay, E., Kanamitsu, M., Kistler, R., Collins, W., Deaven, D., Gandin, L., Iredell, M., Saha, S., White, G., Woollen, J. and Zhu, Y., The NCEP/NCAR 40-year reanalysis project. *Bull. Amer. Meteor. Soc.*, **77**, 437–471, https://doi.org/10.1175/1520-0477(1996)077<0437:TNYRP>2.0.CO;2, 1996.

Kärnä, T. and Baptista, A. M.: Evaluation of a long-term hindcast simulation for the Columbia River estuary, Ocean Model., 99, 1–14, https://doi.org/10.1016/j.ocemod.2015.12.007, 2016.

Kawai, H., Yukimoto, S., Koshiro, T., Oshima, N., Tanaka, T., Yoshimura, H., and Nagasawa, R.: Significant improvement of cloud representation in the global climate model MRI-ESM2, Geosci. Model Dev., 12, 2875–2897, https://doi.org/10.5194/gmd-12-2875-2019, 2019.

Klimont, Z., Kupiainen, K., Heyes, C., Purohit, P., Cofala, J., Rafaj, P., Borken-Kleefeld, J., and Schöpp, W.: Global anthropogenic emissions of particulate matter including black carbon, Atmos. Chem. Phys., 17, 8681–8723, https://doi.org/10.5194/acp-17- 8681-2017, 2017.

Kurylo, M. J. and Soloman, S.: United States NASA Administration Upper Atmosphere Research Program and NOAA Climate and Global Change Program, Network for the Detection of Stratospheric Change: a status and implementation report. Technical report, NASA, Washington, DC, 1990.

Liu, X., Ma, P.-L., Wang, H., Tilmes, S., Singh, B., Easter, R. C., Ghan, S. J., and Rasch, P. J.: Description and evaluation of a new four-mode version of the Modal Aerosol Module (MAM4) within version 5.3 of the Community Atmosphere Model, Geosci. Model Dev., 9, 505–522, https://doi.org/10.5194/gmd-9- 505-2016, 2016.

Lutsch, E., Strong, K., Jones, D. B. A., Blumenstock, T., Conway, S., Fisher, J. A., Hannigan, J. W., Hase, F., Kasai, Y., Mahieu, E., Makarova, M., Morino, I., Nagahama, T., Notholt, J., Ortega, I., Palm, M., Poberovskii, A. V., Sussmann, R., and Warneke, T.: Detection and attribution of wildfire pollution in the Arctic and northern midlatitudes using a network of Fourier-transform infrared spectrometers and GEOS-Chem, Atmos. Chem. Phys., 20, 12813–12851, https://doi.org/10.5194/acp-20-12813-2020, 2020.

Mahieu, E., Fischer, E. V., Franco, B., Palm, M., Wizenberg, T., Smale, D., Clarisse, L., Clerbaux, C., Coheur, P-F., Hannigan, J. W., Lutsch, E., Notholt, J., Pardo Cantos, I., Prignon, M., Servais, C., and Strong, K.: First retrievals of peroxyacetyl nitrate (PAN) from ground-based FTIR solar spectra recorded at remote sites, comparison with model and satellite data, Elementa: Science of the Anthropocene, 9, 00027, https://doi.org/10.1525/elementa.2021.00027 , 2021.

Makar, P., Gong, W., Hogrefe, C., Zhang, Y., Curci, G., Zabkar, R. ., Milbrandt, J., Im, U., Balzarini, A., Baró, R., Bianconi, R., Cheung, P., Forkel, R., Gravel, S., Hirtl, M., Honzak, L., Hou, A., Jiménez-Guerrero, P., Langer, M., Moran, M., Pabla, B., Pérez, J., Pirovano, G., José, R. S., Tuccella, P., Werhahn, J., Zhang, J., and Galmarini, S.: Feedbacks between air pollution and weather, part 2: Effects on chemistry, Atmos. Environ., 115, 499–526, https://doi.org/10.1016/j.atmosenv.2014.10.021, 2015a

Makar, P. A., Gong, W., Milbrandt, J., Hogrefe, C., Zhang, Y., Curci, G., Zabkar, R. ., Im, U., Balzarini, A., Baró, R., Bianconi, R., Cheung, P., Forkel, R., Gravel, S., Hirtl, M., Honzak, L., Hou, A., Jiménez-Guerrero, P., Langer, M., Moran, M., Pabla, B., Pérez, J., Pirovano, G., José, R. S., Tuccella, P., Werhahn, J., Zhang, J., and Galmarini, S.: Feedbacks between air pollution and weather, part 1: Effects on weather, Atmos. Environ., 115, 442–469, https://doi.org/10.1016/j.atmosenv.2014.12.003, 2015b.

Deleted: ,

Marelle, L., Raut, J.-C., Law, K. S., Berg, L. K., Fast, J. D., Easter, R. C., Shrivastava, M., and Thomas, J. L.: Improvements to the WRF-Chem 3.5.1 model for quasi-hemispheric simulations of aerosols and ozone in the Arctic, Geosci. Model Dev., 10, 3661– 3677, https://doi.org/10.5194/gmd-10-3661-2017, 2017.

Marelle, L., Raut, J.-C., Law, K. S., and Duclaux, O.: Current and Future Arctic Aerosols and Ozone From Remote Emissions and Emerging Local Sources—Modeled Source Contributions and Radiative Effects, J. Geophys. Res.-Atmos., 123, 12942–12963, https://doi.org/10.1029/2018JD028863, 2018.

Marsh, D. R., Mills, M. J., Kinnison, D. E., Lamarque, J.-F., Calvo, N., and Polvani, L. M.: Climate Change from 1850 to 2005 Simulated in CESM1 (WACCM), Journal of Climate, 26, 7372–7391, https://doi.org/10.1175/JCLI-D-12-00558.1, 2013.

Massling, A., Nielsen, I. E., Kristensen, D., Christensen, J. H., Sørensen, L. L., Jensen, B., Nguyen, Q. T., Nøjgaard, J. K., Glasius, M., and Skov, H.: Atmospheric black carbon and sulfate concentrations in Northeast Greenland, Atmos. Chem. Phys., 15, 9681–9692, https://doi.org/10.5194/acp-15-9681-2015, 2015.

Monks, S. A., Arnold, S. R., Emmons, L. K., Law, K. S., Turquety, S., Duncan, B. N., Flemming, J., Huijnen, V., Tilmes, S., Langner, J., Mao, J., Long, Y., Thomas, J. L., Steenrod, S. D., Raut, J. C., Wilson, C., Chipperfield, M. P., Diskin, G. S., Weinheimer, A., Schlager, H., and Ancellet, G.: Multi-model study of chemical and physical controls on transport of anthropogenic and biomass burning pollution to the Arctic, Atmos. Chem. Phys., 15, 3575–3603, https://doi.org/10.5194/acp-15-3575-2015, 2015.

Moran, M. D., Pavlovic, R., and Anselmo, D.: Regional air quality deterministic prediction system (RAQDPS): update from version 019 to version 020, Environment and Climate Change Canada, Montreal, https://collaboration.cmc.ec.gc.ca/cmc/CMOI/product_guide/docs/tech_notes/technote_raqdps-v20_20180918_e.pdf (last access: 2 Feb 2023), 2018.

NOAA: Arctic Report Card 2020: Surface Air Temperature, Tech. rep., National Oceanic and Atmospheric Administration (NOAA), Office of Oceanic and Atmospheric Research, Pacific Marine Environmental Laboratory (U.S.), https://doi.org/10.25923/gcw8-2z06, 2020.

Notholt, J., Toon, G., Stordal, F., Solberg, S., Schmidbauer, N., Becker, E., Meier, A., and Sen, B.: Seasonal variations of atmospheric trace gases in the high Arctic at 79∘ N, J. Geophys. Res.-Atmos., 102, 12855–12861, https://doi.org/10.1029/97JD00337, 1997a.

Notholt, J., Toon, G. C., Lehmann, R., Sen, B., and Blavier, J.-F.: Comparison of Arctic and Antarctic trace gas column abundances from ground-based Fourier transform infrared spectrometry, J. Geophys. Res.-Atmos., 102, 12863–12869, https://doi.org/10.1029/97JD00358, 1997b.

Notholt, J., Toon, G. C., Rinsland, C. P., Pougatchev, N. S., Jones, N. B., Connor, B. J., Weller, R., Gautrois, M., and Schrems, O.: Latitudinal variations of trace gas concentrations in the free troposphere measured by solar absorption spectroscopy during a ship cruise, J. Geophys. Res.-Atmos., 105, 1337–1349, https://doi.org/10.1029/1999JD900940, 2000.

Olivié, D., Höglund-Isaksson, L., Klimont, Z., and von Salzen, K.: Boxmodel for calculation of global atmospheric methane concentration, Zenodo, https://doi.org/10.5281/zenodo.5293940, 2021.

Oshima, N., Yukimoto, S., Deushi, M., Koshiro, T., Kawai, H., Tanaka, T. Y., and Yoshida, K.: Global and Arctic effective radiative forcing of anthropogenic gases and aerosols in MRI-ESM2.0, Prog. Earth. Planet. Sci., 7, 38, https://doi.org/10.1186/s40645-020-00348-w, 2020.

Rantanen, M., Karpechko, A.Y., Lipponen, A., Nordling, K., Hyvärinen, O., Ruosteenoja, K., Vihma, T. and Laaksonen, A.: The Arctic has warmed nearly four times faster than the globe since 1979, Commun Earth Environ., **3**, 168, https://doi.org/10.1038/s43247-022-00498-3, 2022.

Prather, M. J., Holmes, C. D., and Hsu, J.: Reactive greenhouse gas scenarios: Systematic exploration of uncertainties and the role of atmospheric chemistry, Geophys. Res. Lett., 39, L09803, https://doi.org/10.1029/2012GL051440, 2012.

Rap, A., Richards, N. A. D., Forster, P. M., Monks, S. A., Arnold, S. R., and Chipperfield, M. P.: Satellite constraint on the tropospheric ozone radiative effect, Geophys. Res. Lett., 42, 5074– 5081, https://doi.org/10.1002/2015GL064037, 2015.

Robertson, L., Langner, J., and Engardt, M.: An Eulerian Limited Area Atmospheric Transport Model, J. Appl. Meteorol., 38, 190– 210, https://doi.org/10.1175/1520-0450(1999)038%3C0190:AELAAT%3E2.0.CO;2, 1999.

Rodgers, C. D.: Inverse Methods for Atmospheric Sounding, pp. 13–100, Atmospheric, Oceanic and Planetary Physics, World Scientific, Singapore, https://doi.org/10.1142/3171, 2000.

Rodgers, C. D. and Connor, B. J.: Intercomparison of remote sounding instruments, Journal of Geophysical Research: Atmospheres, 108, ACH 13, https://doi.org/10.1029/2002JD002299, 2003.

Rodgers, C. D. and Connor, B. J.: Intercomparison of remote sounding instruments, J. Geophys. Res.-Atmos., 108, 4116, https://doi.org/10.1029/2002JD002299, 2003.

Rothman, L., Gordon, I., Barbe, A., Benner, D., Bernath, P., Birk, M., Boudon, V., Brown, L., Campargue, A., Champion, J.-P., Chance, K., Coudert, L., Dana, V., Devi, V., Fally, S., Flaud, J.-M., Gamache, R., Goldman, A., Jacquemart, D., Kleiner, I., Lacome, N., Lafferty, W., Mandin, J.-Y., Massie, S., Mikhailenko, S., Miller, C., Moazzen-Ahmadi, N., Naumenko, O., Nikitin, A., Orphal, J., Perevalov, V., Perrin, A., Predoi-Cross, A., Rinsland, C., Rotger, M., Simeˇckov´a, M., Smith, ˇ M., Sung, K., Tashkun, S., Tennyson, J., Toth, R., Vandaele, A., and Vander Auwera, J.: The HITRAN 2008 molecular spectroscopic database, Journal of Quantitative Spectroscopy and Radiative Transfer, 110, 533–572, https://doi.org/10.1016/j.jqsrt.2009.02.013, 2009.

Scinocca, J. F., McFarlane, N. A., Lazare, M., Li, J., and Plummer, D.: Technical Note: The CCCma third generation AGCM and its extension into the middle atmosphere, Atmos. Chem. Phys., 8, 7055–7074, https://doi.org/10.5194/acp-8-7055-2008, 2008.

Sellar, A. A., Jones, C. G., Mulcahy, J. P., Tang, Y., Yool, A., Wiltshire, A., O'Connor, F. M., Stringer, M., Hill, R., Palmieri, J., Woodward, S., de Mora, L., Kuhlbrodt, T., Rumbold, S. T., Kelley, D. I., Ellis, R., Johnson, C. E., Walton, J., Abraham, N. L., Andrews, M. B., Andrews, T., Archibald, A. T., Berthou, S., Burke, E., Blockley, E., Carslaw, K., Dalvi, M., Edwards, J., Folberth, G. A., Gedney, N., Griffiths, P. T., Harper, A. B., Hendry, M. A., Hewitt, A. J., Johnson, B., Jones, A., Jones, C. D., Keeble, J., Liddicoat, S., Morgenstern, O., Parker, R. J., Predoi, V., Robertson, E., Siahaan, A., Smith, R. S., Swaminathan, R., Woodhouse, M. T., Zeng, G., and Zerroukat, M.: UKESM1: Description and Evaluation of the U.K. Earth System Model, J. Adv. Model. Earth Sy., 11, 4513–4558, https://doi.org/10.1029/2019MS001739, 2019.

Simpson, D., Benedictow, A., Berge, H., Bergström, R., Emberson, L. D., Fagerli, H., Flechard, C. R., Hayman, G. D., Gauss, M., Jonson, J. E., Jenkin, M. E., Nyíri, A., Richter, C., Semeena, V. S., Tsyro, S., Tuovinen, J.-P., Valdebenito, Á., and Wind, P.: The EMEP MSC-W chemical transport model – technical description, Atmos. Chem. Phys., 12, 7825–7865, https://doi.org/10.5194/acp-12-7825-2012, 2012.

Simpson, D., Bergström, R., Tsyro, S., and Wind, P.: Updates to the EMEP MSC-W model, 2018–2019, in: Transboundary particulate matter, photo-oxidants, acidifying and eutrophying components, Emep status report 1/2019, The Norwegian Meteorological Institute, Oslo, Norway, https://emep.int/publ/reports/2019/EMEP_Status_Report_1_2019.pdf, (last access: 2 Feb 2023), 2019.

Skov, H. Brooks, S. Goodsite, M.E. Lindberg, S.E. Meyers, T.P. Landis, M.S. Larsen, M.R.B. Jensen, B. McConville, G. Christensen, J.: Fluxes of reactive gaseous mercury measured with a newly developed method using relaxed eddy accumulation. Atmos. Environ. 40, https://doi.org/10.1016/j.atmosenv.2006.04.061, 5452-5463, 2006.

Solberg, S., Schmidbauer, N., Semb, A., Stordal, F., and Hov, Ø.: Boundary-layer ozone depletion as seen in the Norwegian Arctic in spring, J. Atmos. Chem., 23, 301-332, https://doi.org/10.1007/BF00055158, 1996.

Stohl, A., Aamaas, B., Amann, M., Baker, L. H., Bellouin, N., Berntsen, T. K., Boucher, O., Cherian, R., Collins, W., Daskalakis, N., Dusinska, M., Eckhardt, S., Fuglestvedt, J. S., Harju, M., Heyes, C., Hodnebrog, Ø., Hao, J., Im, U., Kanakidou, M., Klimont, Z., Kupiainen, K., Law, K. S., Lund, M. T., Maas, R., MacIntosh, C. R., Myhre, G., Myriokefalitakis, S., Olivié, D., Quaas, J., Quennehen, B., Raut, J.-C., Rumbold, S. T., Samset, B. H., Schulz, M., Seland, Ø., Shine, K. P., Skeie, R. B., Wang, S., Yttri, K. E., and Zhu, T.: Evaluating the climate and air quality impacts of short-lived pollutants, Atmos. Chem. Phys., 15, 10529–10566, https://doi.org/10.5194/acp-15-10529-2015, 2015.

van der Werf, G. R., Randerson, J. T., Giglio, L., van Leeuwen, T. T., Chen, Y., Rogers, B. M., Mu, M., van Marle, M. J. E., Morton, D. C., Collatz, G. J., Yokelson, R. J., and Kasibhatla, P. S.: Global fire emissions estimates during 1997–2016, Earth Syst. Sci. Data, 9, 697–720, https://doi.org/10.5194/essd-9-697-2017, 2017.

Viatte, C., Strong, K., Hannigan, J., Nussbaumer, E., Emmons, L. K., Conway, S., Paton-Walsh, C., Hartley, J., Benmergui, J., and Lin, J.: Identifying fire plumes in the Arctic with tropospheric FTIR measurements and transport models, Atmos. Chem. Phys., 15, 2227–2246, https://doi.org/10.5194/acp-15-2227-2015, 2015.

Vigouroux, C., Hendrick, F., Stavrakou, T., Dils, B., De Smedt, I., Hermans, C., Merlaud, A., Scolas, F., Senten, C., Vanhaelewyn, G., Fally, S., Carleer, M., Metzger, J.-M., Müller, J.-F., Van Roozendael, M., and De Mazière, M.: Ground-based FTIR and MAX-DOAS observations of formaldehyde at Réunion Island and comparisons with satellite and model data, Atmos. Chem. Phys., 9, 9523–9544, https://doi.org/10.5194/acp-9-9523-2009, 2009.

Wespes, C., Emmons, L., Edwards, D. P., Hannigan, J., Hurtmans, D., Saunois, M., Coheur, P.-F., Clerbaux, C., Coffey, M. T., Batchelor, R. L., Lindenmaier, R., Strong, K., Weinheimer, A. J., Nowak, J. B., Ryerson, T. B., Crounse, J. D., and Wennberg, P. O.: Analysis of ozone and nitric acid in spring and summer Arctic pollution using aircraft, ground-based, satellite observations and MOZART-4 model: source attribution and partitioning, Atmos. Chem. Phys., 12, 237–259, https://doi.org/10.5194/acp-12-237-2012, 2012.

Whaley, C. H., Mahmood, R., von Salzen, K., Winter, B., Eckhardt, S., Arnold, S., Beagley, S., Becagli, S., Chien, R.-Y., Christensen, J., Damani, S. M., Dong, X., Eleftheriadis, K., Evangeliou, N., Faluvegi, G., Flanner, M., Fu, J. S., Gauss, M., Giardi, F., Gong, W., Hjorth, J. L., Huang, L., Im, U., Kanaya, Y., Krishnan, S., Klimont, Z., Kühn, T., Langner, J., Law, K. S., Marelle, L., Massling, A., Olivié, D., Onishi, T., Oshima, N., Peng, Y., Plummer, D. A., Popovicheva, O., Pozzoli, L., Raut, J.-C., Sand, M., Saunders, L. N., Schmale, J., Sharma, S., Skeie, R. B., Skov, H., Taketani, F., Thomas, M. A., Traversi, R., Tsigaridis, K., Tsyro, S., Turnock, S., Vitale, V., Walker, K. A., Wang, M., Watson-Parris, D., and Weiss-Gibbons, T.: Model evaluation of short-lived climate forcers for the Arctic Monitoring and Assessment Programme: a multi-species, multi-model study, Atmos. Chem. Phys., 22, 5775–5828, https://doi.org/10.5194/acp-22-5775-2022, 2022.

Whaley, C., Law, K., Hjorth, J. L., Skov, H., Arnold, S., Langner, J., Pernov, J. B., Chien, R.-Y., Christensen, J., Dong, X., Faluvegi, G., Flanner, M., Fu, J., Gauss, M., Im, U., Marelle, L., Onishi, T., Oshima, N., Plummer, D., Pozzoli, L., Raut, J.-C., Skeie, R., Thomas, M., Tsigaridis, K., Tsyro, S., Turnock, S., von Salzen, K., Tarasick, D., and Worthy, D.: Arctic tropospheric ozone: assessment of current knowledge and model performance., Atmos. Chem. Phys 23, 637–661, https://doi.org/10.5194/acp-23-637-2023, 2023.

Williams, K. D., Copsey, D., Blockley, E. W., Bodas-Salcedo, A., Calvert, D., Comer, R., Davis, P., Graham, T., Hewitt, H. T., Hill, R., Hyder, P., Ineson, S., Johns, T. C., Keen, A. B., Lee, R. W., Megann, A., Milton, S. F., Rae, J. G. L., Roberts, M. J., Scaife, A. A., Schiemann, R., Storkey, D., Thorpe, L., Watterson, I. G., Walters, D. N., West, A., Wood, R. A.,

Woollings, T., and Xavier, P. K.: The Met Office Global Coupled Model 3.0 and 3.1 (GC3.0 and GC3.1) Configurations, J. Adv. Model. Earth Sy., 10, 357– 380, https://doi.org/10.1002/2017MS001115, 2018.

Yukimoto, S., Kawai, H., Koshiro, T., Oshima, N., Yoshida, K., Urakawa, S., Tsujino, H., Deushi, M., Tanaka, T., Hosaka, M., Yabu, S., Yoshimura, H., Shindo, E., Mizuta, R., Obata, A., Adachi, Y., and Ishii, M.: The Meteorological Research Institute Earth System Model Version 2.0, MRI-ESM2.0: Description and Basic Evaluation of the Physical Component, J. Meteorol. Soc. Jpn., 97, 931–965, https://doi.org/10.2151/jmsj.2019-051, 2019.

Zhao, X., Strong, K., Adams, C., Schofield, R., Yang, X., Richter, A., Friess, U., Blechschmidt, A.-M., and Koo, J.-H.: A case study of a transported bromine explosion event in the Canadian high arctic, J. Geophys. Res.-Atmos., 121, 457–477, https://doi.org/10.1002/2015JD023711, 2016.

Zhou, M., Langerock, B., Wells, K. C., Millet, D. B., Vigouroux, C., Sha, M. K., Hermans, C., Metzger, J.-M., Kivi, R., Heikkinen, P., Smale, D., Pollard, D. F., Jones, N., Deutscher, N. M., Blumenstock, T., Schneider, M., Palm, M., Notholt, J., Hannigan, J. W., and De Mazière, M.: An intercomparison of total column-averaged nitrous oxide between ground-based FTIR TCCON and NDACC measurements at seven sites and comparisons with the GEOS-Chem model, Atmos. Meas. Tech., 12, 1393– 1408, https://doi.org/10.5194/amt-12-1393-2019, 2019.